



Available online at www.sciencedirect.com

ScienceDirect

Comput. Methods Appl. Mech. Engrg. 384 (2021) 113932

Computer methods in applied mechanics and engineering

www.elsevier.com/locate/cma

A computational periporomechanics model for localized failure in unsaturated porous media

Shashank Menon, Xiaoyu Song*

Engineering School of Sustainable Infrastructure and Environment, University of Florida, Gainesville, FL 32611, United States of America

Received 28 October 2020; received in revised form 12 May 2021; accepted 14 May 2021

Available online 17 June 2021

Abstract

This article is devoted to a computational plastic periporomechanics model for localized failure in unsaturated porous media assuming passive atmospheric pressure. The computational periporomechanics model is formulated based on the hypothesis that unsaturated porous media can be represented by a collection of two-phase material points with infinitesimal volumes interacting with each other within finite distance. The effective force state concept for solid skeleton deformation and the peridynamic state concept for unsaturated fluid flow are utilized in the coupled integro-differential field equations that have an intrinsic length scale. The unsaturated fluid flow state and effective force state are determined by the fluid potential state and the deformation state of the solid skeleton, respectively. The periporomechanics model is numerically implemented by an implicit two-phase meshfree method in which the message passing interface technique is used for parallel computing. The numerical implementation is validated by simulating classical coupled poromechanics problems and comparing numerical results with analytical solutions and experimental data. Numerical examples under different scenarios are conducted to demonstrate the robustness of the implemented computational periporomechanics model for simulating localized failure in unsaturated porous media as a coupled solid deformation and unsaturated fluid flow problem.

© 2021 Elsevier B.V. All rights reserved.

Keywords: Periporomechanics; Coupled; Localized failure; Unsaturated porous media; Nonlocal; Parallel computing

1. Introduction

Strain localization of geomaterials is a significant problem because it is closely related to the onset of failure of geomaterials (e.g., [1–7]). For example, the failure of soil slopes is a typical strain localization problem in which deformation usually occurs in a narrow banded zone with a finite thickness [8,9]. The thickness of shear bands in geomaterials can be in the order of several grain sizes as observed in the laboratory testing [10–13] or be of the scale of meters in the field [14]. Strain localization in solid materials is characterized by the concentration of strain or displacement discontinuity in a narrow banded zone. Mathematically, strain localization is a bifurcation problem from a continuous deformation to a discontinuous one. Over the past decades, numerous studies of shear banding have been focused on fluid saturated geomaterials. In recent years, strain localization in unsaturated soils has been a subject of tremendous interest because of the importance of practical engineering applications (e.g., unsaturated

^{*} Corresponding author.

E-mail address: xysong@ufl.edu (X. Song).

soil slope failure and geothermal energy production and storage) (e.g., [9,15,16]). Unsaturated soils are three-phase porous media consisting of a deformable solid skeleton, pore water, and pore air [17–19]. Strain localization in unsaturated soils involves the coupled solid deformation and unsaturated fluid flow process (e.g., [20–24]). Numerical methods such as the finite element method [25,26] are useful tools to study the triggering mechanisms of strain localization in unsaturated geomaterials (e.g., [27–29]). The numerical results via the nonlinear mixed finite element method have shown that the multiphase material heterogeneity (e.g., density and degree of saturation) can be the first-order trigger on shear banding in unsaturated geomaterials (e.g., [30,31]).

The finite element method has difficulties (e.g., mesh sensitivity) in modeling the propagation of localized failures. From the mathematical viewpoint, one underlying reason is the loss of ellipticity of the partial differential equation at the onset of shear bands [32]. Typical regularization techniques for overcoming the ill-posedness problem include rate-dependent models, higher-order gradient models, nonlocal models, the strong discontinuity approach, phase-field models, and the extended finite element method (e.g., [33-36]). Recently these remedies for modeling single-phase materials have been applied to simulate shear bands in multiphase materials (e.g., [23,37–41], among others). Ehlers and Luo [39] proposed a phase-field approach embedded in the theory of porous media for modeling dynamic hydraulic fracturing. Oka et al. [23] developed an elasto-viscoplastic model for strain localization analysis of unsaturated soils under dynamic conditions. Roth et al. [40] presented a three-dimensional extended finite element model for application to complex flow in discontinuities. Those enhanced finite element methods for modeling shear bands except the nonlocal models or models with an embedded length scale usually assume a zero thickness of shear bands. However, a length scale is usually needed to realistically model the formation of shear bands at the continuum scale. In general, there are also physical reasons for formulating a nonlocal continuum framework for modeling materials in general and unsaturated porous media in particular. The physical reasons may include heterogeneity of microstructures and its homogenization [42], grain or pore size and geometrical effects [43], length scales of modeling fluid flow in porous media at the continuum scale through averaging theory and upscaling methods [44,45], and solid-fluid interaction at the nanoscale considering long-range forces [46-48].

To better model shear bands with finite thickness in unsaturated geomaterials as a two-phase discontinuity problem, a novel candidate technique is the state-based peridynamics. Peridynamics is a nonlocal reformulation of continuum theory for solid materials through integro-differential equations that are valid at discontinuities such as shear bands [49,50]. It is noted that the bond-based and ordinary state-based peridynamics are special cases of the state-based peridynamics (or the so-called non-ordinary state-based peridynamics). Thus, by peridynamics here we mean the state-based peridynamics. Major development of peridynamics theory has been focused on modeling single-phase solid materials (e.g., [51-64], among many others). In recent years, peridynamics has been used to study the fluid flow or coupled fluid flow and deformation problems (e.g., [65-74]). Turner [65] proposed a peridynamic model accounting for fluid-structure interaction for modeling fractures in which the fluid pressure was given. Jabakhanji et al. [67] proposed a bond-based peridynamics formulation for fluid flow in porous media. Katiyar et al. [75] formulated a peridynamic model for fluid flow in porous media assuming rigid skeleton. In [68] a coupled poroelastic peridynamic model was presented to simulate fluid-driven fractures in poroelastic materials. In [70], a peridynamic elastoplastic model for unsaturated geomaterials under drained condition was formulated through the original correspondence principle for single-phase solid materials [50]. In [73], the model in [68] was implemented by an implicit method to model consolidation and dynamic problems in saturated soils. In [74], a hybrid finite element and peridynamic model was proposed to simulate hydraulic fracture propagation in saturated porous media. In [76], the authors proposed the effective force state concept and a multiphase constitutive correspondence principle for modeling deformable three-phase porous media through stated-based peridynamics. In [76], simple numerical samples under drained condition (e.g., pore water pressure is uncoupled) were presented to test their hypothesis that unsaturated geomaterials can be modeled as a single-phase peridynamic material through the effective force state concept.

In this article, as a new contribution we implement and validate a fully coupled computational plastic periporomechanics model for unsaturated porous media. The mathematical model in the form of integro-differential equations is formulated based on the peridynamic effective force concept for unsaturated porous media [76] and the peridynamic state concept for unsaturated fluid flow [50]. The intrinsic two-phase length scale in the field equations can be utilized to capture the finite thickness of shear bands coupled with unsaturated fluid flow. Here the intrinsic two-phase length scale means that a length scale exists in both the solid skeleton deformation and fluid flow field equations. For numerical implementation, the governing equations are discretized in space by a two-phase

Lagrangian meshfree method extended from [77] and in time by a fully implicit method [25]. Due to its nonlocal formulation, the periporomechanics model is computationally more demanding than numerical methods based on classical theory. To circumvent this problem, here Open MPI [78,79] is utilized to boost the implemented numerical model for high-performance computing. The validation of the numerical implementation has been accomplished by simulating Terzaghi's one-dimensional consolidation problem, drainage of a soil column, and Mandel's slab problem [80–82] and comparing the numerical results with the analytical solutions and experimental data. Numerical simulations of localized failure in unsaturated porous media under different scenarios are performed through the implemented computational periporomechanics model. The detailed numerical results and analysis demonstrate that the computational periporomechanics model is robust in simulating strain localization in unsaturated porous media as a coupled solid skeleton deformation and unsaturated fluid flow problem.

The article is organized as follows. Section 2 introduces the periporomechanics model for unsaturated porous media assuming a passive atmospheric pressure under quasi-static conditions. Section 3 presents the numerical implementation via an implicit two-phase Lagrangian meshfree method. Section 4 deals with the validation of the numerical implementation. Section 5 presents numerical simulations of localized failure in unsaturated soils via the implemented periporomechanics model, followed by a summary in Section 6. Sign convention in continuum mechanics is adopted, i.e., the tensile stress in solid is positive, and pore fluid pressure in compression is positive.

2. Mathematical model

In this section, we present a periporomechanics model for unsaturated soils under quasi-static condition assuming passive air pressure and incompressible solid grains. We note that peridynamics can be used to study static problems although it was originally proposed to study dynamic problems in solids. The scope of this study is to model strain localization in unsaturated soils under static conditions. For dynamic strain localization of solids and porous media, we refer to the classical literature (e.g., [83–85]). For the sake of notation and nomenclature, we briefly introduce the effective stress concept of classical poromechanics for unsaturated soil (e.g., [18,86]). The difference between pore air and pore water pressures in unsaturated soil is usually called matric suction. Here, it is assumed that pore air pressure in unsaturated soils is at equilibrium with external atmospheric pressure (i.e., passive pore air pressure). In this case, matric suction is merely negative pore water pressure. Following this assumption, the general form of the effective stress for the solid skeleton (e.g., [87–89]) is written as

$$\bar{\sigma} = \sigma + \bar{S}_r p_w \mathbf{1},\tag{1}$$

where $\bar{\sigma}$ is the effective Cauchy stress tensor, σ is the total Cauchy stress tensor and p_w is the pore water pressure, 1 is the second-order identity tensor, and \bar{S}_r is the effective degree of saturation [89] defined as

$$\bar{S}_r = \frac{S_r - S_1}{S_2 - S_1},\tag{2}$$

where S_r is the degree of saturation, S_1 and S_2 are the residual and maximum degree of saturation, respectively. In unsaturated poromechanics, the degree of saturation can be determined through the soil-water retention curve [90] given matric suction (i.e., negative pore water pressure). Without loss of generality, the soil-water retention curve is represented by van Genuchten equation [91].

$$S_r = S_1 + (S_2 - S_1) \left[1 + \left(\frac{-p_w}{s_a} \right)^n \right]^{-m}, \tag{3}$$

where s_a is a scaling factor, and m and n are fitting parameters for the experimental data. Given the soil water retention curve, the relative permeability of the pore water phase [92] is expressed as

$$k_w^r = S_r^{1/2} \left[1 - \left(1 - S_r^{1/m} \right)^m \right]^2,$$
 (4)

where m is the same parameter in (3).

In the periporomechanics model, it is hypothesized that unsaturated porous media can be represented by a collection of material points (solid skeleton and pore water) with infinitesimal volumes that interact with each other at finite distance. A material point x in a body \mathcal{B} interacts with other materials points x' within its neighborhood called the *family* of x, denoted \mathcal{H}_x [50]. The radius of the neighborhood is called the *horizon*, δ . The interaction between material points is generally called a "bond". The Lagrangian coordinate system is adopted for the solid

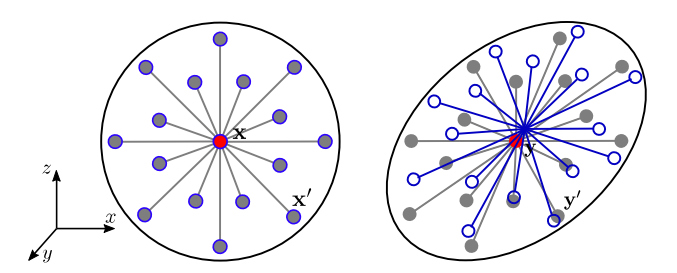


Fig. 1. Schematic of a solid material point (in gray and red) and a pore water material point (in blue) and their corresponding neighboring material points within \mathcal{H}_x : reference state (left) and deformed state (right). (For interpretation of the references to color in this figure legend, the reader is referred to the web version of this article.)

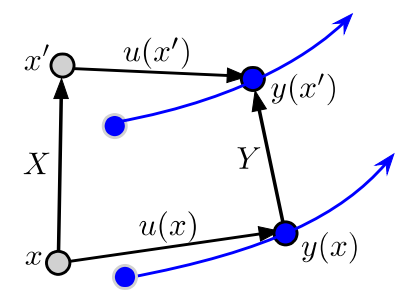


Fig. 2. Schematic of kinematics of the solid skeleton and pore fluid material points (solid material point in black and fluid material point in blue). (For interpretation of the references to color in this figure legend, the reader is referred to the web version of this article.)

material points and the relative Eulerian coordinate system moving with respect to the solid phase is employed for the pore fluid material points (see Fig. 1). Fig. 1 shows a schematic of a material point and other material points in its neighborhood \mathcal{H}_x in the reference and the deformed configuration. In the periporomechanics model, the fundamental peridynamic states consist of the solid deformation vector state, the effective force vector state, fluid flow scalar state, and pore pressure scalar state. Peridynamic states that are mathematical objects applying to continuous or discontinuous functions depend upon position and time and operate on a vector connecting two material points. Depending on whether the value of this operation is a scalar or vector, a peridynamic state is called a scalar state or a vector state. For instance, the deformation state is a function that maps any mechanical bond onto its image under the deformation. The effective force state contains the effective forces within mechanical bonds of all lengths and orientations that are imposed on the solid skeleton.

Fig. 2 sketches the kinematics of the solid skeleton and pore fluid phases in the periporomechanics framework. The relative position of the solid skeleton material points x and x' in the reference configuration is given by the reference position vector X denoted as the bond vector ξ

$$X = x' - x = \xi, \quad \text{and } \xi' = x - x'. \tag{5}$$

In the following, a variable with a prime means that the parameter is evaluated at material point x'. The relative position of the same solid material points in the deformed configuration is given by the deformation position vector state Y

$$Y = y' - y, (6)$$

where y' and y are the position vectors of the solid material points x' and x, respectively, in the deformed configuration. Let u = u(x) and u' = u(x') be the displacements of material points x and x', respectively. It follows

$$\mathbf{y} = \mathbf{x} + \mathbf{u}, \quad \text{and} \quad \mathbf{y}' = \mathbf{x}' + \mathbf{u}'. \tag{7}$$

The displacement vector states at material points x and x' along bonds ξ and ξ' respectively are

$$U = u' - u, \quad \text{and} \quad U' = u - u'. \tag{8}$$

The pore water pressure states at material points x and x' in the current configuration are defined as

$$\Phi_w = p'_w - p_w, \text{ and } \Phi'_w = p_w - p'_w,$$
(9)

where p'_w and p_w are pore water pressures at material points x' and x, respectively in the current configuration. Assuming a passive pore air pressure the total force state for unsaturated porous media through the effective force concept can be defined as

$$T = \overline{T} + \overline{S}_r T_w, \tag{10}$$

where T is the total force state, \overline{T} is the effective force state that is an energy conjugate to the deformation state of the solid skeleton [76], and T_w is the force state of pore water, which is related to pore water pressure. Given (10) the linear momentum balance of unsaturated porous media assuming passive air pressure under the quasi-static condition at material point x can be written as

$$\int_{\mathcal{H}_{s}} \left[\left(\overline{T} + \overline{S}_{r} T_{w} \right) - \left(\overline{T}' + \overline{S}_{r}' T_{w}' \right) \right] dV' + \left[\rho_{s} (1 - \phi) + \rho_{w} \phi S_{r} \right] g = 0, \tag{11}$$

where ρ_s is the intrinsic density of the soil solid, ρ_w is the intrinsic density of pore water, ϕ is the porosity of the mixture, and g is the gravity acceleration vector. Assuming that the soil solid grain is incompressible, the mass balance equation at material point x can be written as

$$\phi \frac{\mathrm{d}S_r}{\mathrm{d}t} + \frac{\phi S_r}{K_w} \frac{\mathrm{d}p_w}{\mathrm{d}t} + S_r \int_{\mathcal{H}_r} \left(\dot{\mathcal{V}}_s - \dot{\mathcal{V}}_s'\right) \mathrm{d}V' + \frac{1}{\rho_w} \int_{\mathcal{H}_r} \left(\widetilde{Q}_w - \widetilde{Q}_w'\right) \mathrm{d}V' = 0, \tag{12}$$

where K_w is the bulk modulus of pore water, $\dot{\mathcal{V}}_s$ and $\dot{\mathcal{V}}_s'$ are the rates of volume change scalar state of the solid skeleton at material points \boldsymbol{x} and \boldsymbol{x}' , respectively, \widetilde{Q}_w and \widetilde{Q}_w' are the mass flow scalar states of pore water relative to the solid skeleton at material points \boldsymbol{x} and \boldsymbol{x}' , respectively. Material models for the solid skeleton deformation and unsaturated fluid flow are needed to complete (11) and (12).

In the computational periporomechanics model, the constitutive and physical models for the solid deformation and unsaturated fluid flow are cast into the above framework through the multiphase constitutive correspondence principle [76], putting it into the category of the non-ordinary peridynamics model. It is noted that the so-called bond-based and ordinary state-based peridynamics models which are special cases of the non-ordinary peridynamics model can be formulated following the same lines in [49,50]. The total force state of the mixture reads

$$T = \omega \left(\overline{\sigma} - \overline{S}_r p_w \mathbf{1} \right) J \widetilde{F}^{-T} \mathcal{K}^{-1} \boldsymbol{\xi}, \tag{13}$$

where the weighting function is expressed as $\underline{\omega}$ for brevity, and J is Jacobian (determinant) of \widetilde{F} . The effective stress $\overline{\sigma}$ can be determined by a classical elastoplastic constitutive model for unsaturated soils given \widetilde{F} [70]. Here the nonlocal deformation gradient can be determined from the deformation state Y as

$$\widetilde{F} = (Y * X)\mathcal{K}^{-1} = \left(\int_{\mathcal{H}_{x}} \underline{\omega} Y \otimes X \, dV_{x'}\right) \mathcal{K}^{-1},\tag{14}$$

where the symbol '*' is the peridynamic equivalent of the tensor-product and K is the peridynamic shape tensor [50] that is defined as

$$\mathcal{K} = \int_{\mathcal{H}_x} \underline{\omega} \boldsymbol{\xi} \otimes \boldsymbol{\xi} \, dV'. \tag{15}$$

Given (13), Eq. (11) can be written as

$$\int_{\mathcal{H}_{x}} \left[\left(\underline{\omega} \left(\overline{\sigma} - \overline{S}_{r} p_{w} \mathbf{1} \right) J \widetilde{F}^{-T} \mathcal{K}^{-1} \xi \right) - \left(\underline{\omega} \left(\overline{\sigma}' - \overline{S}'_{r} p'_{w} \mathbf{1} \right) J \widetilde{F}^{-T} \mathcal{K}^{-1} \xi' \right) \right] dV'
+ \left[\rho_{s} (1 - \phi) + \rho_{w} \phi S_{r} \right] g = \mathbf{0}.$$
(16)

Similarly, the mass flow state for the pore water at material point x can be defined as

$$\widetilde{Q}_w = \omega \rho_w J \mathbf{q}_w \mathcal{K}^{-1} \boldsymbol{\xi}. \tag{17}$$

where q_w is the volume flux of the pore water at material point x. It can be determined by the generalized Darcy's law for unsaturated fluid flow [93] as

$$\boldsymbol{q}_{w} = -k_{w}^{r} k \mathbf{1} \widetilde{\boldsymbol{\nabla}} \boldsymbol{\Phi}_{w}, \tag{18}$$

where k is the hydraulic conductivity for pore water and k_w^r is the relative permeability of pore water under unsaturated condition as defined in (4), and $\widetilde{\nabla} \Phi_w$ is the nonlocal pore water pressure gradient at material point x in the current configuration. The latter is determined from the pore water pressure state as

$$\widetilde{\nabla \Phi}_w = \left(\int_{\mathcal{H}_X} \underline{\omega} \Phi_w X \, dV' \right) \mathcal{K}^{-1}. \tag{19}$$

Given (17), Eq. (12) can be written as

$$\phi \frac{\mathrm{d}S_r}{\mathrm{d}t} + \frac{\phi S_r}{K_w} \frac{\mathrm{d}p_w}{\mathrm{d}t} + S_r \int_{\mathcal{H}_r} \left(\underline{\omega} \dot{\mathbf{y}} \mathcal{K}^{-1} \boldsymbol{\xi} - \underline{\omega} \dot{\mathbf{y}}' \mathcal{K}^{-1} \boldsymbol{\xi}' \right) \mathrm{d}V' + \int_{\mathcal{H}_r} \left(\underline{\omega} J \boldsymbol{q}_w \mathcal{K}^{-1} \boldsymbol{\xi} - \underline{\omega} J \boldsymbol{q}_w' \mathcal{K}^{-1} \boldsymbol{\xi}' \right) \mathrm{d}V' = 0. \quad (20)$$

Th first two rate terms in Eq. (20) are the same as in the classical poromechanics for unsaturated soils and only the divergence terms are replaced by peridynamic formulations in line with a nonlocal vector calculus [50,94]. All the input material parameters in the constitutive and physical models for the solid skeleton and fluid phases are measurable variables due to the adopted multiphase constitutive correspondence principle.

In the periporomechanics model, the boundary and loading conditions do not mathematically emerge. The boundary conditions are usually prescribed in the form of volumetric constraints in a nonlocal region of thickness δ (i.e., a fictitious boundary layer) along the boundary of a nonzero body [49,57,76]. The essential boundary conditions (i.e., displacement or pore fluid pressure) can be prescribed at the material points in a fictitious region along the problem domain boundary, constraining the solution in a nonzero volume. The natural boundary conditions (i.e., traction force or pore fluid flux) can be applied through a force or flow density at material points in a boundary layer along the boundary of a nonzero porous material volume. For example, the fluid flow density can be computed by equating the fluid flow along the boundary surface as in classical local poromechanics to the fluid flow through a nonlocal region of a fictitious boundary layer along the boundary. The application of a zero fluid flow boundary condition can be achieved by assigning a zero-valued fluid flow density in material points in the fictitious boundary layer.

3. Numerical implementation

This section concerns the numerical implementation of the periporomechanics model for unsaturated porous media. As elaborated in the previous section, the mathematical formulation of the periporomechanics model is based on the hypothesis that a body of unsaturated porous media consists of mixed material points. In line with this hypothesis, the integro-differential equations of the periporomechanics model can be discretized by a multiphase Lagrangian meshless method in spatial domain. In temporal domain, a fully implicit method is adopted [25]. In the proposed method, the problem domain is discretized into a finite number of equal-sized mixed material points (i.e., pore fluid and solid skeleton). Each material point has two kinds of degrees of freedom, i.e., displacement and pore fluid pressure. Thus, the two-phase meshless method is an extended version of the one in [77,95] that is for modeling single-phase solid materials. We refer to the literature for technical details on computational meshfree methods (e.g., [96], among others). We note that the implemented periporomechanics model is computationally more demanding than the classical poromechanics model due to nonlocality. Thus, high-performance computing is essential. The message passing interface technique [78,79] is utilized to enhance the implemented computational periporomechanics model for high-performance computing. Note that the mixed peridynamics and finite element model could be a computationally more efficient method than the fully coupled periporomechanics method for modeling large-scale engineering problems [74,97]. For coupling peridynamics with the finite element method, we refer to the literature (e.g., [74,97–99], among others).

3.1. Implicit time integration

An implicit time integration algorithm is employed for the unsaturated periporomechanics model. The fundamental unknowns at a mixed material point are displacement vector \mathbf{u} and pore water pressure p_w . Given the values of displacement vector and pore water pressure at time step n, the fully implicit time integration [25] is used to determine the displacement vector and pore water pressure at time step n+1. At time step n+1, we can write out the momentum balance as

$$\mathcal{G}_{n+1} = \int_{\mathcal{H}_{\boldsymbol{x}}} \left[\left(\overline{\boldsymbol{T}} - \bar{S}_r \boldsymbol{T}_w \right) - \left(\overline{\boldsymbol{T}}' - \bar{S}_r' \boldsymbol{T}_w' \right) \right] dV' + \left[\rho_s (1 - \phi) + \rho_w \phi S_r \right] \boldsymbol{g} = \boldsymbol{0}, \tag{21}$$

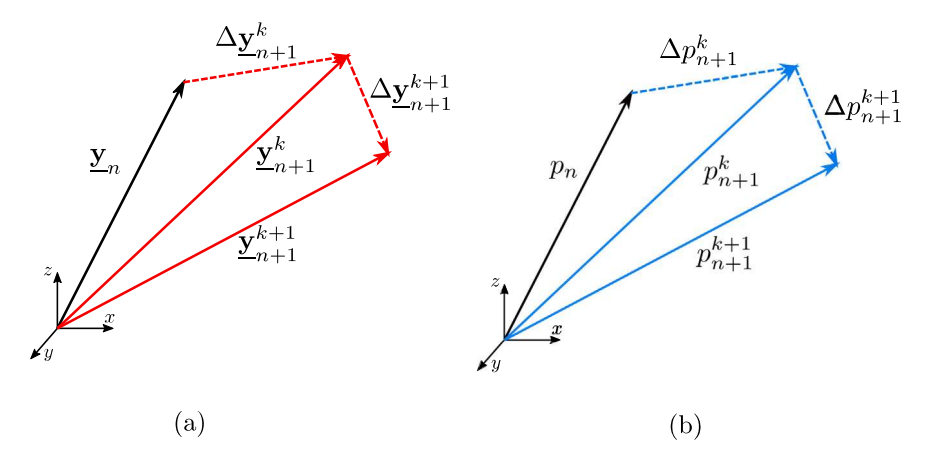


Fig. 3. Incremental kinematics for the solid phase and the pore water pressure of the fluid phase. Note: k and k+1 are iteration numbers at time step n+1.

where the variables at mixed material points x and x' are evaluated at time step n+1, and the subscript n+1 is omitted for brevity. The effective force state at time step n+1 is determined by the effective stress through (13). Given the nonlocal deformation gradient, the effective stress is computed from the elastoplastic constitutive model for unsaturated soils summarized in the Appendix. In line with the global implicit time integration, this elastoplastic constitutive model is numerically implemented through an implicit algorithm (e.g., [30,100–103]). We refer to [71] for the algorithm of implementing the constitutive model at a material point.

The backward finite difference is adopted to approximate the rate terms of the mass balance equation in time domain. Then we have

$$\widetilde{\mathcal{M}}_{n+1} = \left(\frac{\phi S_r}{K_w} - \phi \frac{\partial S_r}{\partial p_w}\right) \frac{p_w - p_{w,n}}{\Delta t} + S_r \int_{\mathcal{H}_x} \left[\underline{\omega} \frac{\mathbf{y} - \mathbf{y}_n}{\Delta t} \mathcal{K}^{-1} \boldsymbol{\xi} - \underline{\omega} \frac{\mathbf{y}' - \mathbf{y}'_n}{\Delta t} \mathcal{K}^{-1} \boldsymbol{\xi}'\right] dV' + \int_{\mathcal{H}_x} \left[\underline{\omega} \boldsymbol{q}_w \mathcal{K}^{-1} \boldsymbol{\xi} - \underline{\omega} \boldsymbol{q}'_w \mathcal{K}^{-1} \boldsymbol{\xi}'\right] dV' = 0,$$
(22)

where a subscript n+1 for variables at time step n+1 is omitted for brevity, and variables at time step n are noted with a subscript n. Multiplying Δt on both sides of Eq. (22) generates

$$\mathcal{M}_{n+1} = \left(\frac{\phi S_r}{K_w} - \phi \frac{\partial S_r}{\partial p_w}\right) (p_w - p_{w,n}) + S_r \int_{\mathcal{H}_x} \left[\underline{\omega}(\mathbf{y} - \mathbf{y}_n) \mathcal{K}^{-1} \boldsymbol{\xi} - \underline{\omega}(\mathbf{y}' - \mathbf{y}_n') \mathcal{K}^{-1} \boldsymbol{\xi}'\right] dV' + \Delta t \int_{\mathcal{H}_x} \left[\underline{\omega} \boldsymbol{q}_w \mathcal{K}^{-1} \boldsymbol{\xi} - \underline{\omega} \boldsymbol{q}_w' \mathcal{K}^{-1} \boldsymbol{\xi}'\right] dV' = 0.$$
(23)

3.2. Linearization

The tangent stiffness matrix is required when solving nonlinear equations by Newton's method. In general, the tangent stiffness matrix is a function of the chosen linearization point and must be updated every time step when the nodal degrees of freedom (displacement and pore water pressure) are updated. The tangent stiffness matrix relates an infinitesimal disturbance in the degree of freedom to change in the global force state and the global fluid flow state. For the coupled periporomechanics model the tangent stiffness matrix contains non-zero entries for each node that interacts directly as well as nodes that share a neighbor material point, which makes the Jacobian inherently denser than that of a classic coupled poromechanics model. Fig. 3 sketches the incremental kinematics for the solid phase and the pore fluid phase, respectively.

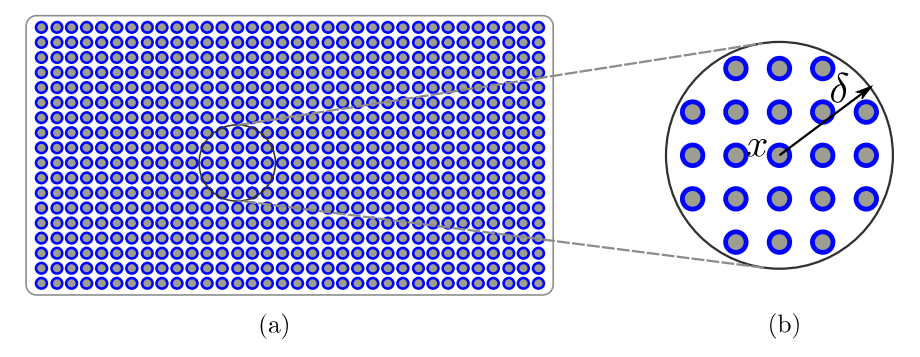


Fig. 4. (a) Schematic of the multiphase meshfree spatial discretization of an unsaturated porous material body, and (b) zoom-in view of material point x and its neighbors within \mathcal{H}_x . Note: the gray dot represents the solid skeleton and the blue circle represents the pore water. (For interpretation of the references to color in this figure legend, the reader is referred to the web version of this article.)

The linearization of the momentum balance equation with respect to the displacement vector states U and U', and the pore water pressures p_w and p'_w at time step n+1 assuming an infinitesimal deformation is

$$\delta \mathbf{\mathcal{G}}_{n+1} = \int_{\mathcal{H}_{x}} \left(\frac{\partial \overline{T}}{\partial U} \bullet \delta U - \frac{\partial \overline{T}'}{\partial U'} \bullet \delta U' \right) dV'$$

$$- \int_{\mathcal{H}_{x}} \left[\left(\mathbf{T}_{w} \frac{\partial \overline{S}_{r}}{\partial p_{w}} + \overline{S}_{r} \frac{\partial \mathbf{T}_{w}}{\partial p_{w}} \right) \delta p_{w} - \left(\mathbf{T}'_{w} \frac{\partial \overline{S}_{r}}{\partial p'_{w}} + \overline{S}_{r} \frac{\partial \mathbf{T}'_{w}}{\partial p'_{w}} \right) \delta p'_{w} \right] dV' + \rho_{w} \phi \mathbf{g} \frac{\partial S_{r}}{\partial p_{w}} \delta p_{w} = \mathbf{0}, \quad (24)$$

where • is the dot product operator for peridynamic states [50].

Similarly, the linearization of the mass balance equation at time step n + 1 is

$$\delta \mathcal{M}_{n+1} = S_r \int_{\mathcal{H}_x} \left[\underline{\omega} (\mathcal{K}^{-1} \boldsymbol{\xi}) \delta \boldsymbol{U} - \underline{\omega} (\mathcal{K}^{-1} \boldsymbol{\xi}') \delta \boldsymbol{U}' \right] dV' + \left[\left(\frac{\phi S_r}{K_w} - \phi \frac{\partial S_r}{\partial p_w} \right) + \left(\frac{\phi}{K_w} \frac{\partial S_r}{\partial p} - \phi \frac{\partial^2 S_r}{\partial p_w^2} \right) \Delta p_w \right] \delta p_w$$

$$+ \int_{\mathcal{H}_x} \left[\underline{\omega} (\mathcal{K}^{-1} \boldsymbol{\xi}) \Delta \boldsymbol{y} - \underline{\omega} (\mathcal{K}^{-1} \boldsymbol{\xi}') \Delta \boldsymbol{y}' \right] dV' \frac{\partial S_r}{\partial p_w} \delta p_w$$

$$+ \Delta t \int_{\mathcal{H}_x} \left[\underline{\omega} (\mathcal{K}^{-1} \boldsymbol{\xi}) \frac{\partial \boldsymbol{q}_w}{\partial \Phi_w} \delta \Phi_w - \underline{\omega} (\mathcal{K}^{-1} \boldsymbol{\xi}') \frac{\partial \boldsymbol{q}_w'}{\partial \Phi_w'} \delta \Phi_w' \right) dV' = 0.$$

$$(25)$$

3.3. Multiphase meshfree spatial discretization

Fig. 4 sketches the two-phase meshfree discretization of a problem domain. For a material point i, it is assumed that there are totally k material points within its family \mathcal{H}_x . As elaborated earlier, both material point i and its neighboring material points have two kinds of degree of freedom, the displacement of solid skeleton and the pressure of pore water. The momentum balance equation at material point i becomes

$$\mathcal{G}_{i} = \sum_{j=1}^{k} \left[\left(\overline{\boldsymbol{T}}_{i} - \bar{\boldsymbol{S}}_{r,i} \boldsymbol{T}_{w,i} \right) - \left(\overline{\boldsymbol{T}}_{j}^{\prime} - \bar{\boldsymbol{S}}_{r,j}^{\prime} \boldsymbol{T}_{w,j}^{\prime} \right) \right] V_{j}^{\prime} + \left[\rho_{s} (1 - \phi_{i}) + \rho_{w} \phi_{i} S_{r,i} \right] \boldsymbol{g} = \boldsymbol{0}, \tag{26}$$

where V'_j is the volume of material point j within the *family* of material point i. It is noted that in the sum operator the variable with subscript i means that the variable is imposed on material point i and operate on the bond ξ_{ij} . Similarly, the mass balance equation at material point i is

$$\mathcal{M}_{i} = \left(\frac{\phi_{i} S_{r,i}}{K_{w}} - \phi_{i} \frac{\partial S_{r,i}}{\partial p_{w,i}}\right) \Delta p_{w,i} + S_{r,i} \sum_{j=1}^{k} \left[\underline{\omega} \Delta(\mathbf{y}_{i}) \mathcal{K}_{i}^{-1} \boldsymbol{\xi}_{i} - \underline{\omega} (\Delta \mathbf{y}_{j}') \mathcal{K}_{j}^{-1} \boldsymbol{\xi}_{j}'\right] V_{j}'$$

$$+ \Delta t \sum_{j=1}^{k} \left[\underline{\omega} \boldsymbol{q}_{w,i} \mathcal{K}_{i}^{-1} \boldsymbol{\xi}_{i} - \underline{\omega} \boldsymbol{q}_{w,j}' \mathcal{K}_{j}^{-1} \boldsymbol{\xi}_{j}'\right] V_{j}' = 0.$$

$$(27)$$

At time step n + 1, the linearization of the momentum balance is

$$\delta \mathbf{\mathcal{G}}_{i} = \sum_{j=1}^{k} \left(\frac{\partial \overline{\mathbf{T}}_{i}}{\partial \mathbf{U}_{i}} \bullet \delta \mathbf{U}_{i} - \frac{\partial \overline{\mathbf{T}}_{j}'}{\partial \mathbf{U}_{j}'} \bullet \delta \mathbf{U}_{j}' \right) V_{j}' + \rho_{w} \phi_{i} \mathbf{g} \frac{\partial S_{r,i}}{\partial p_{w,i}} \delta p_{w,i}$$

$$- \sum_{j=1}^{k} \left[\left(\mathbf{T}_{w,i} \frac{\partial \overline{S}_{r,i}}{\partial p_{i}} + \overline{S}_{r,i} \frac{\partial \mathbf{T}_{w,i}}{\partial p_{w,i}} \right) \delta p_{w,i} - \left(\mathbf{T}_{w,j}' \frac{\partial \overline{S}_{r,j}}{\partial p_{w,j}'} + \overline{S}_{r,j} \frac{\partial \mathbf{T}_{w,j}'}{\partial p_{w,j}'} \right) \delta p_{w,j}' \right] V_{j}' = \mathbf{0}.$$
(28)

Similarly, the spatial discretization of the linearized mass balance equation is

$$\delta \mathcal{M}_{i} = S_{r,i} \sum_{j=1}^{k} \left[\underline{\omega} (\mathcal{K}_{i}^{-1} \boldsymbol{\xi}_{i}) \delta \boldsymbol{y}_{i} - \underline{\omega} (\mathcal{K}_{j}^{-1} \boldsymbol{\xi}_{j}') \delta \boldsymbol{y}_{j}' \right] V_{j}' + \left[\left(\frac{\phi_{i} S_{r,i}}{K_{w}} - \phi_{i} \frac{\partial S_{r,i}}{\partial p_{w,i}} \right) + \left(\frac{\phi_{i}}{K_{w}} \frac{\partial S_{r,i}}{\partial p_{w,i}} - \phi_{i} \frac{\partial^{2} S_{r,i}}{\partial p_{w,i}^{2}} \right) \Delta p_{w,i} \right] \delta p_{w,i}$$

$$+ \sum_{i}^{k} \left[\underline{\omega} (\mathcal{K}_{i}^{-1} \boldsymbol{\xi}_{i}) \Delta \boldsymbol{y}_{i} - \underline{\omega} (\mathcal{K}_{j}^{-1} \boldsymbol{\xi}_{j}') \Delta \boldsymbol{y}_{j}' \right] V_{j}' \frac{\partial S_{r,i}}{\partial p_{w,i}} \delta p_{w,i}$$

$$+ \Delta t \sum_{j=1}^{k} \left[\underline{\omega} (\mathcal{K}_{i}^{-1} \boldsymbol{\xi}_{i}) \frac{\partial \boldsymbol{q}_{w,i}}{\partial \Phi_{w,i}} \bullet \delta \Phi_{w,i} - \underline{\omega} (\mathcal{K}_{j}^{-1} \boldsymbol{\xi}_{j}') \frac{\partial \boldsymbol{q}'_{w,j}}{\partial \Phi'_{w,j}} \bullet \delta \Phi'_{w,j} \right] V_{j}' = 0. \tag{29}$$

The tangent matrix is assembled by looping over all the individual material points and their neighbors and it accounts for the effect of perturbations in all degrees of freedom in every single bond on the force state and the fluid flow state at the material point. The linearization is considered for the material point itself as well as all its neighbors for each degree of freedom such as the displacement and the pore water pressure. Parallel computing capability of the implemented numerical model is accomplished through Open MPI, an open-source MPI (message passing interface) library [77,95]. Here MPI is a communication protocol for programming parallel computers. We refer to [78,79] for the technical details regarding the implementation of Open MPI for high-performance computing.

4. Validation of the numerical implementation

This section validates the implemented computational periporomechanics model by conducting numerical simulations of Terzaghi's one-dimensional consolidation problem, the drainage of a soil column, and Mandel's slab problem [80–82]. We note that all boundary conditions in the numerical examples are prescribed through the boundary layer approach in peridynamics.

4.1. Terzaghi's one-dimensional consolidation

Terzaghi's one-dimensional consolidation problem is simulated, and the numerical result is compared against the analytical solution. For the soil specimen, the height is 20 cm, the width is 5 cm, and the out-of-plane thickness is 1 cm. Both lateral boundaries are constrained against horizontal deformation and are free to deform vertically. The bottom boundary is fixed in all three directions. The problem domain is discretized into 400 material points with a characteristic dimension of $\Delta x = 0.5$ cm. The horizon δ is taken as $2\Delta x$. The soil skeleton is assumed as a homogeneous elastic material with bulk modulus $K = 8.3 \times 10^4$ kPa and shear modulus $G = 1.8 \times 10^4$ kPa. The fluid density ρ_w is 1000 kg/m³ and is assumed incompressible. The hydraulic conductivity of the soil skeleton k is 1×10^{-8} m/s and the initial porosity is $\phi = 0.5$. The initial and boundary conditions for the fluid phase are as follows. For the initial state, all boundaries for the fluid phase are impervious. The top boundary is prescribed with a zero fluid pressure (i.e., the atmospheric pressure) during the consolidation process. A surcharge in the form of force density, equivalent to 50 kPa, is applied on the top boundary at t=0 s and is held constant during the simulation. The total simulation time is 2000 s with an equal time step $\Delta t = 1$ s. Fig. 5(a) plots the excess pore water pressure from the numerical simulation with the analytical solution at different consolidation stages [80]. Fig. 5(b) shows an m-convergence analysis of the numerical solution. Here m is the ratio of the horizon to the characteristic length of the material point (i.e., Δx). The m-convergence is performed by repeating the simulation assuming the same horizon with different spatial discretization schemes. It is shown from Fig. 5 that the numerical solution is in good agreement with the analytical solution and the numerical results are insensitive to the spatial discretization given the same horizon.

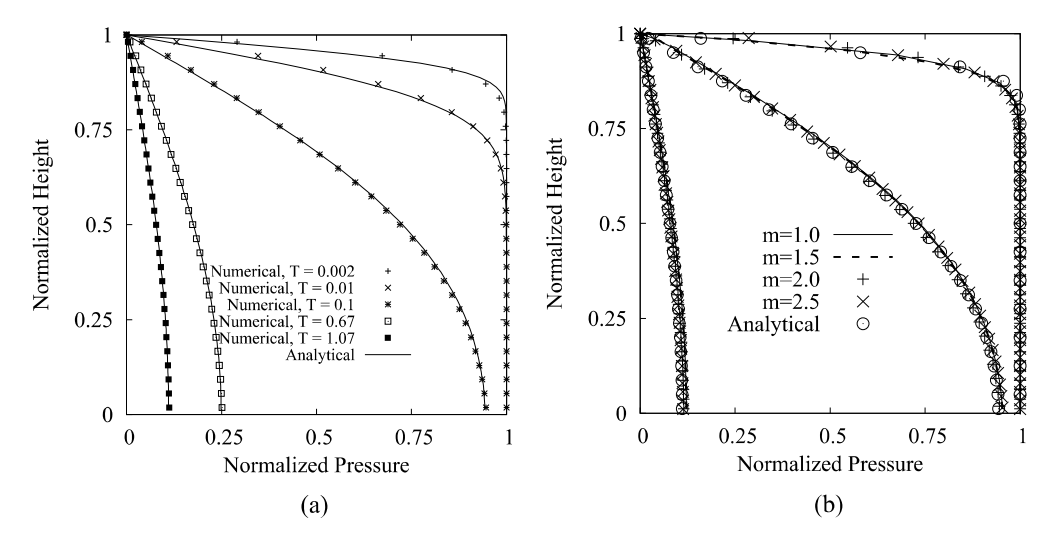


Fig. 5. (a) Numerical and analytical solutions of excess water pressure versus the height of the soil specimen at different consolidation times. (b) m-convergence of the periporomechanics solution to the analytical solution. Note: T is the dimensionless time factor in [80].

4.2. Drainage of a soil column

This example is about the laboratory experiment of drainage of a sand column [81]. The numerical results are compared with the experimental data. The sand column is 1 m in height and 0.25 m in width. The sample is discretized into uniform material points with a characteristic length of $\Delta x = 0.2$ m. The horizon δ is assumed as $2\Delta x$. For the material parameters, Young's modulus is 1.3 MPa, Poisson's ratio is 0.4, soil density is 2000 kg/m³, water density is 1000 kg/m³, porosity is 0.2975, and intrinsic permeability is 4.5×10^{-10} m². From the data provided by Liakopoulos, the degree of saturation and the relative permeability of water are approximated by the following equations [87].

$$S_r = 1 - (1.9722 \times 10^{-11})(-p_w)^{2.4279},\tag{30}$$

$$k_r = 1 - 2.207(1 - S_r)^{1.021}$$
 (31)

For the solid phase, the lateral surfaces are constrained against lateral displacement but free to deform vertically, and the bottom is constrained for vertical displacement. For the fluid phase, both the upper and lower ends of the column are exposed to atmospheric pressure, and zero flux conditions are imposed on the lateral surfaces. The sand column is initially fully saturated with water. The water drainage is solely driven by the gravity load. The results are plotted in Fig. 6. In Fig. 6(a) the pore water pressure from numerical simulations at different times is compared to the experimental results. The numerical results are in good agreement with the experimental data except for the early-stage results. During the earlier stages the pore water pressure predicted by the numerical analysis decreases more rapidly than the laboratory testing results. At t = 20 and 30 min, the numerical results of pore water pressure are in better agreement with the experimental data. Fig. 6(b) shows that the fluid flow velocity at the specimen bottom from the numerical result is close to the experimental data. It is noted that the numerical result generally does not match the experiment data exactly since the input parameters from the literature are approximate ones obtained by trial and error (e.g., [20,87]).

4.3. Mandel's slab problem

In this example, Mandel's slab problem is simulated to examine if the implemented computational periporomechanics model can capture the Mandel–Cryer effect under saturated condition [82,104]. The Mandel–Cryer effect is a non-monotonic pore fluid pressure response that can only be captured by a fully coupled poromechanics model. Fig. 7 sketches Mandel's slab problem. The same material parameters for the Terzaghi's consolidation in 4.1 are adopted. The specimen is 10 m in width, 3 m in height, and 0.4 m in depth. The specimen is discretized into 1500

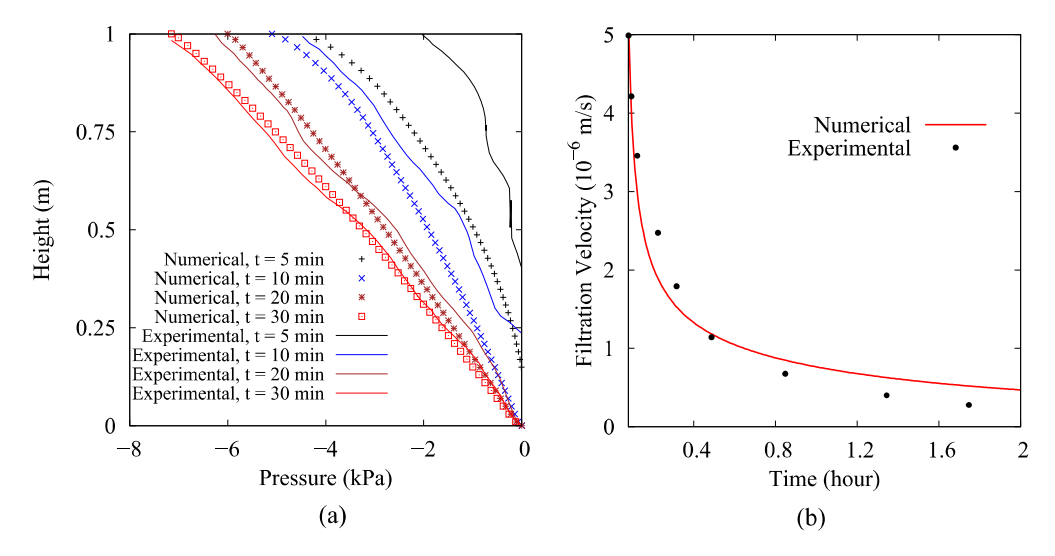


Fig. 6. Comparison of the numerical results and experimental data [81] of (a) water pressure in the soil column at different times and (b) variation of fluid filtration velocity at the base of the column over time.

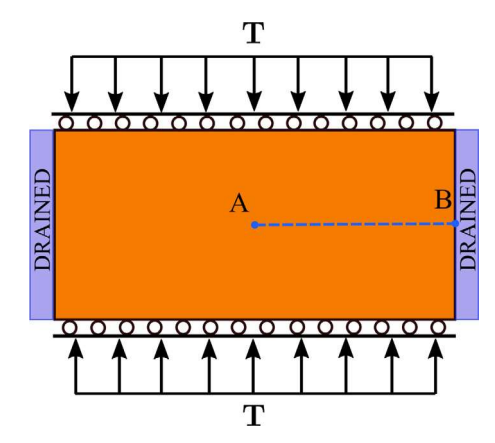


Fig. 7. Sketch of the model setup, loading protocol and boundary conditions (Note: T is the external load).

equal-sized material points with $\Delta x = 0.2$ m. The horizon $\delta = 0.4$ m. The initial excess pore fluid pressure is 1 kPa. At t = 0, the fluid pressure at both lateral boundaries is set to zero, and a vertical surcharge equivalent to 1 kPa is prescribed on the top. The numerical result is compared against the analytical solution [82,105]. Fig. 8 plots the variation of the water pressure at point A. Fig. 8(b) plots the variation of the pore water pressure along the line AB at three different times. It is shown that the numerical results are in good agreement with the analytical solution. Thus, it can be concluded that the coupled periporomechanics model can capture the Mandel-Cryer effect observed in classical poromechanics.

5. Numerical examples

Numerical examples of localized failure in unsaturated soils under different scenarios are presented in this section. Example 1 is a shear and compression test of a two-dimensional unsaturated soil sample. Example 2 concerns strain localization in a simple compression test under two-dimensional condition. Examples 1 and 2 study the influence of the horizon on shear bands. Meanwhile, example 2 also analyzes the impact of the hydraulic conductivity and spatial discretization on the numerical results. Example 3 simulates the bearing capacity of a footing on unsaturated soils. For all examples, the same intrinsic length scale (i.e., horizon) is adopted for both the fluid and solid phases.

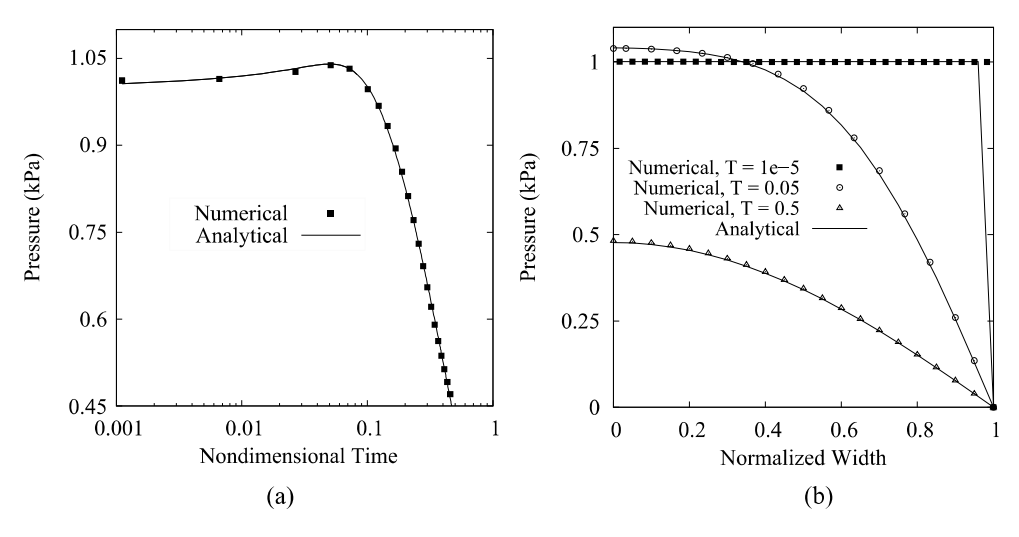


Fig. 8. Comparison of the numerical and analytical solutions of (a) water pressure at the point A at the center of Mandel's slab and (b) along the line AB at three non-dimensional times.

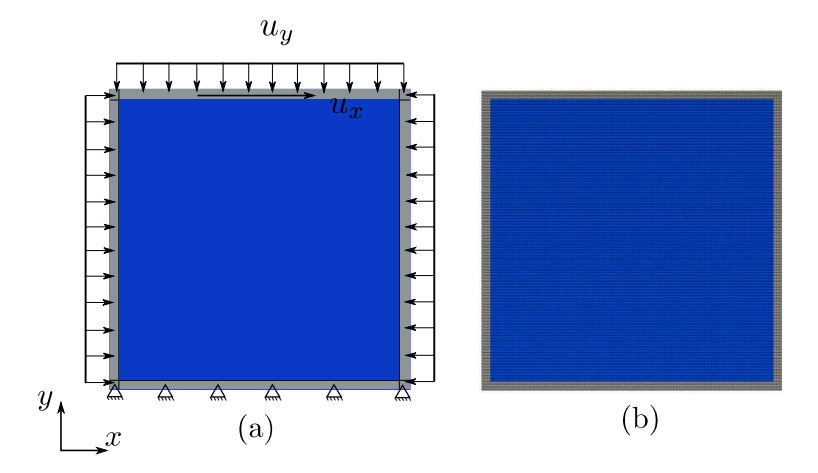


Fig. 9. (a) Model setup, and (b) spatial discretization (the problem domain in blue and the boundary layers in gray).

For simplicity, the unit weighting function is used for all terms in the mathematical model [50]. All boundary and loading conditions are imposed on the material points within the fictitious boundary layer of thickness δ .

5.1. Example 1: Shear and compression of a two-dimensional specimen

In this example, we simulate a two-dimensional unsaturated soil specimen under combined shear and compression loading. As shown in Fig. 9(a), the soil specimen is 1 cm by 1 cm in the x-y plane and the out-of-plane thickness is 0.025 cm. The sample is discretized into 12,800 material points with a characteristic length $\Delta x = 0.125$ mm. Fig. 9(b) sketches the spatial discretization. The horizon δ is 0.25 mm and the thickness of boundary layers is 0.25 mm. The material parameters for the solid skeleton are assumed as follows: bulk modulus is 38.9 MPa, shear modulus is 13 MPa, swelling index is 0.03, slope of critical state line is 1.0, compression index is 0.12, specific volume at unit preconsolidation pressure is 2.76, and fitting parameters for preconsolidation pressure [70] are 0.185 and 1.42. The parameters for soil water characteristic curve are $S_1 = 0.0$, $S_2 = 1.0$, $S_a = 20$ kPa, $S_a = 2.0$, $S_a =$

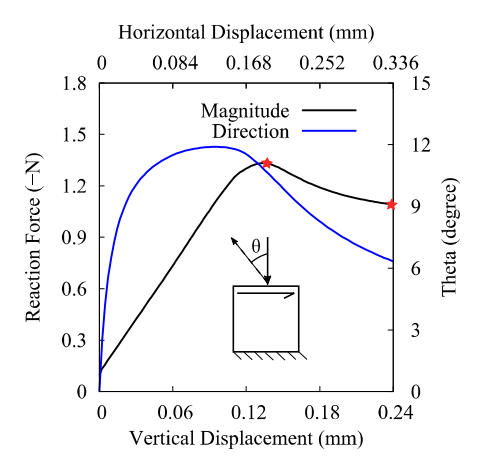


Fig. 10. Reaction force and its direction versus the vertical and horizontal displacements at the top boundary. Note the markers at displacements: $u_y = 0.13$ mm and $u_y = 0.24$ mm.

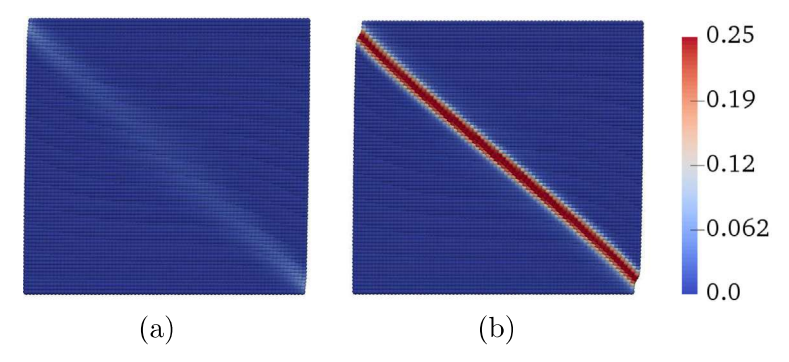


Fig. 11. Contours of equivalent plastic shear strain at displacements: (a) $u_v = 0.13$ mm and (b) $u_v = 0.24$ mm.

The bottom of the specimen is fixed. All fluid phase boundaries are impervious. For the initial state, a uniform isotropic stress state with a magnitude of -100 kPa is prescribed on the skeleton, and apparent pre-consolidation pressure is -300 kPa. In the sample, the initial suction is assumed 20 kPa, and the degree of saturation is 0.8. The constant confining pressure on the lateral boundaries is 84 kPa, which is imposed through an equivalent total force density [71]. For the loading protocol, the soil specimen is subjected to a vertical compression load and an in-plane shear load on the top boundary. Both loads are prescribed by constant displacement rates of 1×10^{-5} m/s in the y direction and 1.4×10^{-5} m/s in the x direction, respectively (see Fig. 9). The confining pressure is applied on both lateral boundaries by a linear ramp function in 0.04 s. Then, the external loads are imposed on the top boundary with the prescribed constant rates. The total simulation time is 24 s.

Fig. 10 plots the reaction force versus the vertical and horizontal displacements at the top boundary, as well as the direction of the reaction force and its eventual variation with increasing displacement. The markers in Fig. 10 denote the vertical displacements: $u_y = 0.14$ mm and $u_y = 0.24$ mm, respectively. The results of plastic strains, pore water pressure and fluid flux vector for the load steps are shown in Figs. 11–14. Fig. 11 shows the contours of equivalent plastic shear strain (i.e., the second invariant of the plastic deviator strain tensor [27]). It is noted that the boundary layers are omitted here. Fig. 12 plots the contours of plastic volume strain. The results in both figures demonstrate that a single shear band with a finite thickness has been initiated and developed in the specimen. The soil skeleton experiences positive plastic volumetric strain in the localized shear zone. Thus, it can be concluded that the shear band is a dilative one. Fig. 13 plots the pore water pressure at the selected load steps. The results in Fig. 13 show that a single banded zone has formed in the contour of pore water pressure. The banded zone of pore water pressure is consistent with the shear band of the solid skeleton shown in Figs. 11 and 12. The decrease

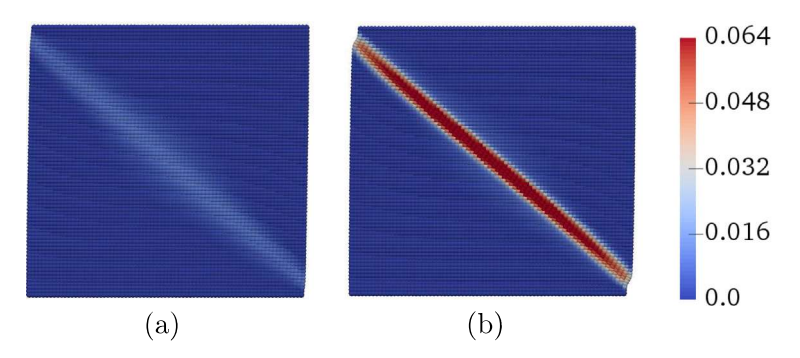


Fig. 12. Contours of plastic volumetric strain at displacements: (a) $u_y = 0.13$ mm and (b) $u_y = 0.24$ mm.

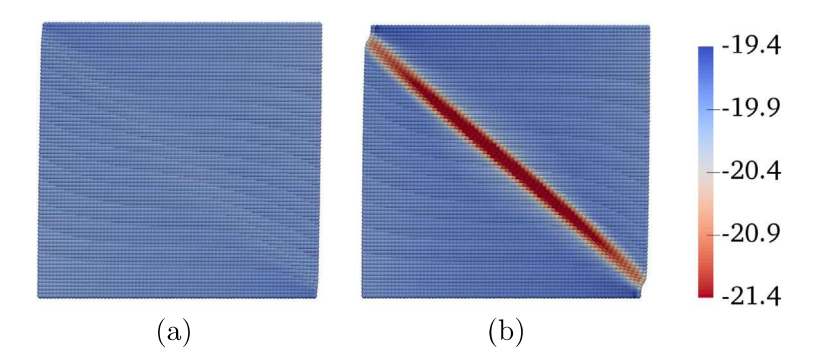


Fig. 13. Contours of pore water pressure (kPa) at displacements: (a) $u_y = 0.13$ mm and (b) $u_y = 0.24$ mm.

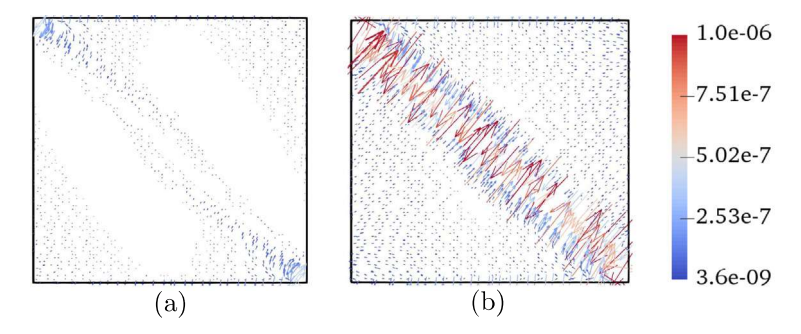


Fig. 14. Contours of fluid flux vector and the magnitude at displacements: (a) $u_y = 0.13$ mm and (b) $u_y = 0.24$ mm.

in the pore water pressure inside the shear band (equivalently, suction increases) can be in part due to the plastic dilation in the banded deformation zone.

Fig. 14 plots the snapshots of the fluid flux vector on the undeformed configuration at the selected load steps. The results demonstrate that the water flows into the center of the specimen at the inception of shear banding. After the shear band occurs, more water flows into the banded zone. This can be due to the fact that the pore water pressure in the banded zone is lower than the pore water pressure outside the shear band (refer to Fig. 13). As the plastic volumetric strain (see Fig. 12) increases in the banded zone, the pore water pressure decreases and the magnitude of the water flux rises because of the increased difference (or discontinuity) between the pore water pressures within and outside the shear band. It can be concluded from the example that the proposed periporomechanics model can capture the finite thickness of the shear band and the localized zone of the water pressure in the specimen.

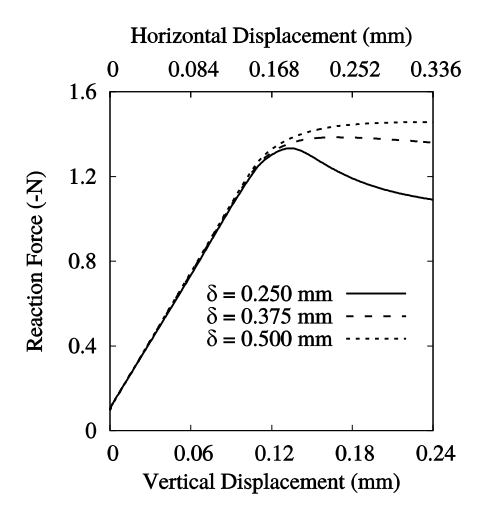


Fig. 15. Comparison of reaction force for the cases of $\delta=0.25$ mm, $\delta=0.375$ mm and $\delta=0.5$ mm.

5.1.1. Influence of horizon

The horizon δ in the proposed periporomechanics is an intrinsic length scale for both the fluid and solid phases. The impact of the horizon on the formation of shear banding under shear and compression conditions is examined here. In so doing, we re-run the simulation in Section 5.1 with two more horizons, $\delta = 0.375$ mm and $\delta = 0.5$ mm while keeping all other simulation parameters unchanged. Fig. 15 compares the loading capacity curves (the reaction force versus displacement) generated by the simulations with the three horizons, respectively. The results show that the peak reaction forces (or applied loads) are different for the simulations with these three horizons. It is evident that the force responses are almost identical at the early loading stages. After the peak load, the loading curves diverge, which demonstrates the load capacity of the specimen in the post-localized regime is sensitive to the intrinsic length scale (horizon). Specifically, the simulation with a larger horizon (e.g., $\delta = 0.5$ mm) generates a relatively larger loading capacity in the post-localization regime. Figs. 16 and 17 plot the contours of equivalent plastic shear strain and pore water pressure at the vertical displacement = 0.24 mm, respectively. The results obviously show that the internal length scale impacts both the formation of shear deformation band and pore pressure band. The simulation with $\delta = 0.25$ mm (the smallest horizon in all three cases) produces the narrowest shear band and the maximum intensity of strain and pore water pressure within the shear band in all three cases. From the results in Figs. 15–17, it may be concluded that the deformation pattern, pore water pressure distribution, and the load capacity of the specimen are all dependent on the horizon size in the numerical model. For instance, under the same other conditions, the simulation with a larger horizon generates less intense plastic deformation in the localized zone than the simulation with a smaller horizon. Furthermore, the results show that the horizon may be correlated to the finite thickness of the shear band. It may imply that the proposed periporomechanics model can better capture the thickness of shear bands in unsaturated soils by adjusting the horizon.

5.2. Example 2: Compression of a two-dimensional specimen

In this example, we conduct a compression test of a two-dimensional unsaturated soil specimen with a constant confining pressure. Fig. 9(a) sketches the problem domain and the displacement loading condition. The specimen has the same geometrical size as the one for Example 1 (Fig. 9(a)) in 5.1. The bottom is fixed in all directions. Both lateral boundaries are prescribed with constant confining pressure. All fluid phase boundaries are impervious. The specimen is discretized into 12,800 equal-sized material points with a characteristic length $\Delta x = 0.125$ mm. The horizon δ is 0.25 mm. For the initial state, a uniform isotropic stress state of -100 kPa is prescribed on the skeleton, and apparent pre-consolidation pressure is -300 kPa. The initial suction is 20 kPa. Equivalently, the pore water pressure is -20 kPa. The constant confining pressure on the lateral boundaries is 84 kPa, which is imposed through an equivalent total force density [71]. For the loading protocol, the confining pressure is applied by a linear

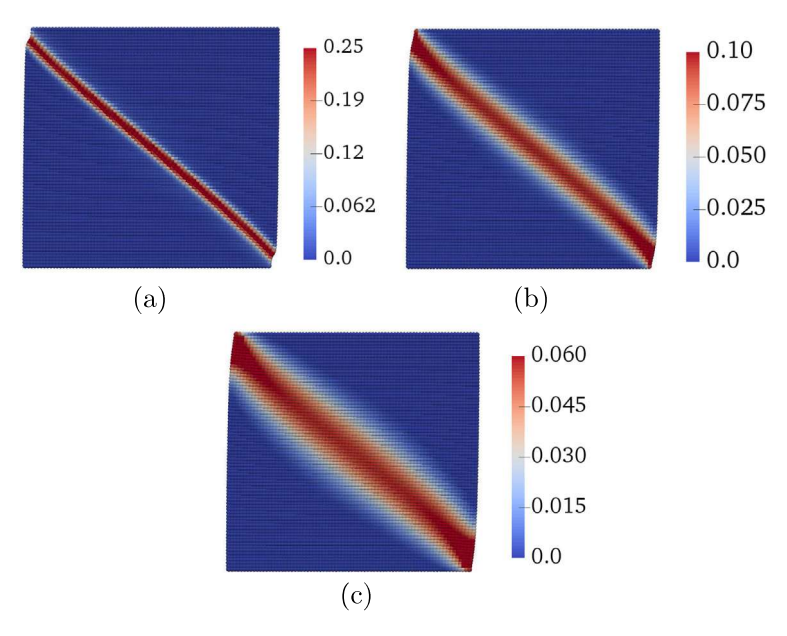


Fig. 16. Contours of equivalent plastic shear strain at the applied displacement $u_y = 0.24$ mm for (a) $\delta = 0.25$ mm, (b) $\delta = 0.375$ mm, and (c) $\delta = 0.5$ mm.

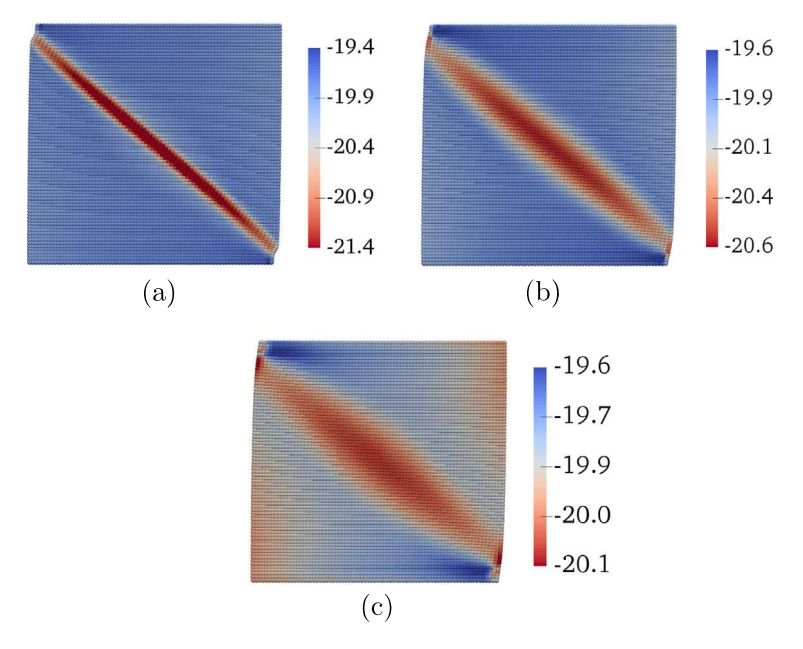


Fig. 17. Contours of pore water pressure (kPa) at the applied displacement $u_y = 0.24$ mm for (a) $\delta = 0.25$ mm, (b) $\delta = 0.375$ mm, and (c) $\delta = 0.5$ mm.

ramp function in 0.04 s. Then, the top boundary is subjected to a vertical compression with a rate of 3×10^{-5} m/s. The total simulation time is 24 s.

Fig. 18 plots the reaction force versus the vertical displacement of the top boundary. The markers in Fig. 18 correspond to two applied displacements: (a) $u_y = 0.18$ mm and (b) $u_y = 0.72$ mm, respectively. The peak reaction force occurs at $u_y = 0.18$ mm. Simulation results at both load stages are shown in Figs. 19–22. All contours depicted here are drawn on the deformed configuration of the specimen. Fig. 19 presents the snapshots of equivalent

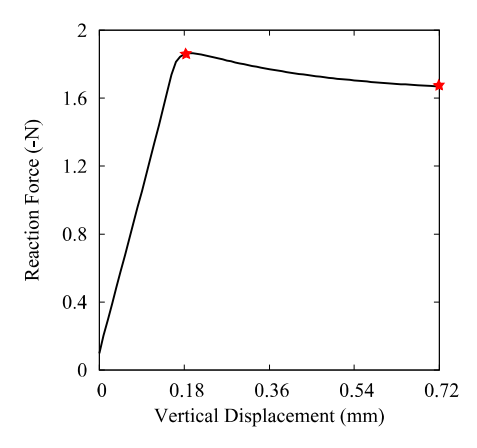


Fig. 18. Reaction force versus the vertical displacement at the top boundary.

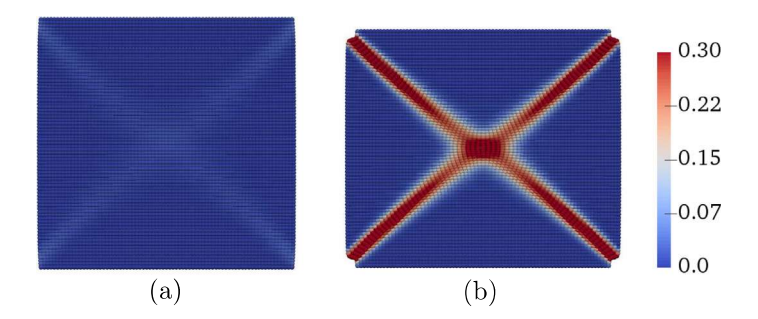


Fig. 19. Contours of equivalent plastic shear strain at displacements: (a) $u_y = 0.18$ mm and (b) $u_y = 0.72$ mm.

plastic shear strain. The results show the formation of two conjugate shear bands in the specimen. Fig. 20 presents the snapshots of the plastic volumetric strains. The results in Fig. 20 show that positive plastic volumetric strains occur in localized shear zones. Fig. 21 presents the snapshots of pore water pressure. Similar to the results for the deformation field in Figs. 19 and 20, two conjugate banded zones have formed in the pore water pressure field. Within the shear band, the pore water pressure is smaller than that outside the shear band. It is also evident that both the deformation band and the fluid pressure band have a similar finite thickness in that the same horizon is adopted for both the solid and the fluid. Fig. 22 shows the snapshots of the fluid flux vector and the magnitude at the different load stages. The results show that the pore water flows into the shear band. This is due to the fact that the pore water within the shear band decreases (or equivalently suction increases) in the formation of dilative shear bands.

5.2.1. Influence of horizon

We study the influence of the horizon on the formation of shear bands under the symmetrical loading condition. In so doing, the previous simulation is repeated with two more horizons, $\delta=0.375$ mm and $\delta=0.5$ mm while keeping all other parameters unchanged. Fig. 23 compares the loading capacity curves (i.e., the applied loads versus the vertical displacement the top boundary) generated by the simulations with the three horizons, respectively. The results show that the loading response curves are slightly sensitive to the horizon size in the post-localization regime. The simulation with a larger horizon size generates a higher loading response at the same load step.

Figs. 24 and 25 show the contours of pore water pressure and plastic shear strain at the last load step of the simulations with the three horizons. Similar to the results of the shear example, the horizon size can influence the deformation and pore water pressure in the post-localization regime (e.g., the thickness of shear bands and the

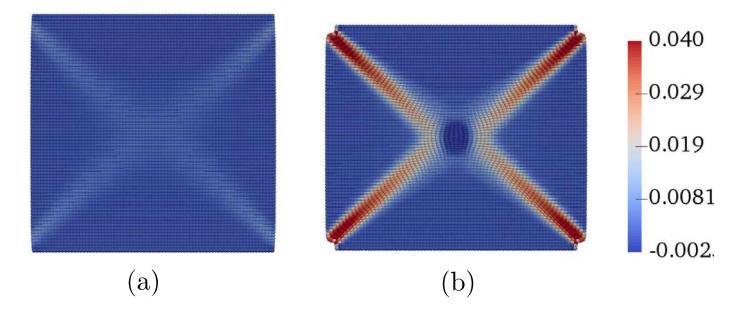


Fig. 20. Contours of plastic volume strain at displacements: (a) $u_y = 0.18$ mm and (b) $u_y = 0.72$ mm.

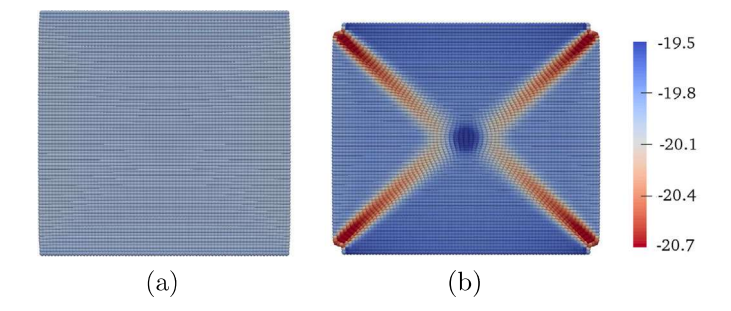


Fig. 21. Contours of pore water pressure (kPa) at displacements: (a) $u_y = 0.18$ mm and (b) $u_y = 0.72$ mm.

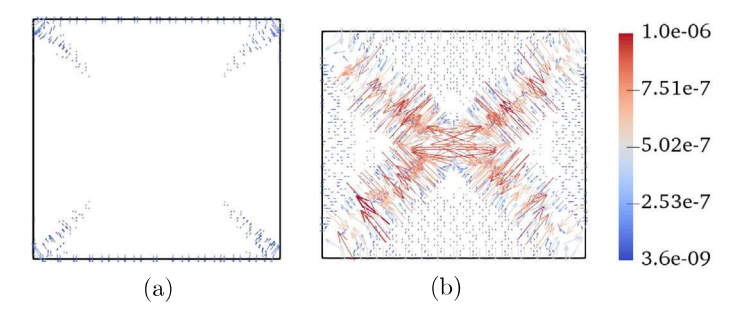


Fig. 22. Contours of fluid flow vector and the magnitude at displacements: (a) $u_y = 0.18$ mm and (b) $u_y = 0.72$ mm.

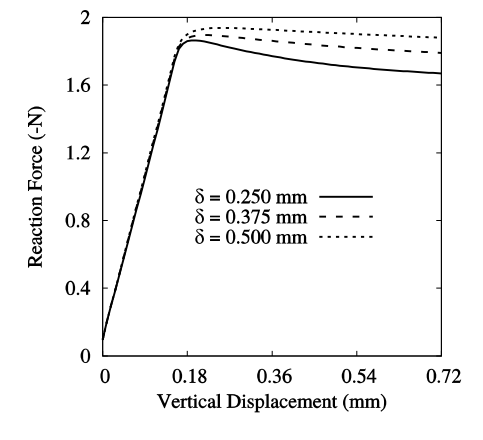


Fig. 23. Comparison of force versus applied vertical displacement for $\delta=0.25$ mm, (b) $\delta=0.375$ mm, and (c) $\delta=0.5$ mm.

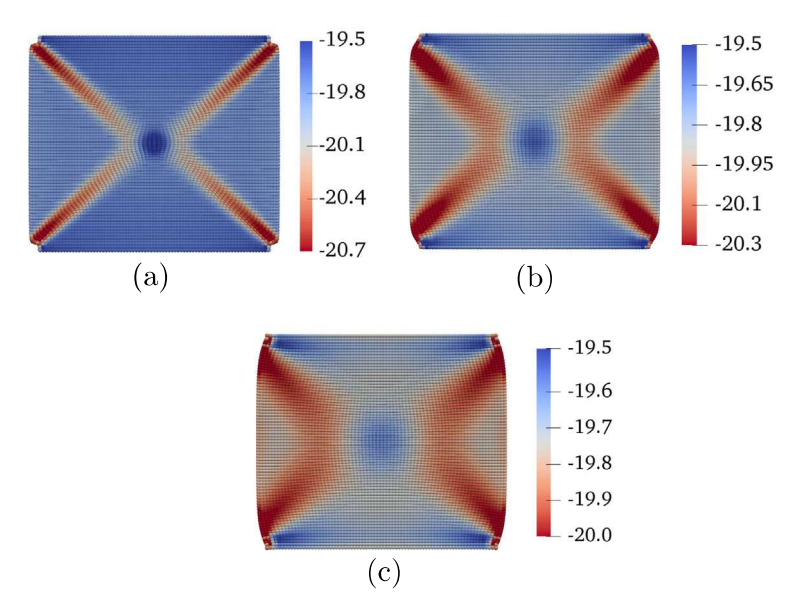


Fig. 24. Contours of pore water pressure at $u_v = 0.72$ mm for (a) $\delta = 0.25$ mm, (b) $\delta = 0.375$ mm, and (c) $\delta = 0.5$ mm.

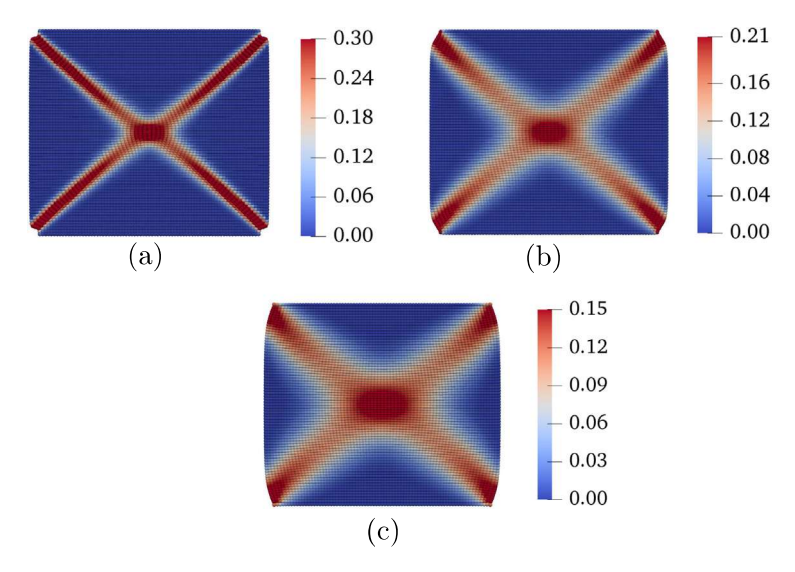


Fig. 25. Contours of equivalent plastic shear strain at $u_y = 0.72$ mm for (a) $\delta = 0.25$ mm, (b) $\delta = 0.375$ mm, and (c) $\delta = 0.5$ mm.

magnitude of the pore water pressure in the shear band). For instance, the simulation with the smallest horizon size generates the most intense plastic shear strain within the shear bands.

5.2.2. Influence of hydraulic conductivity

We analyze the influence of the hydraulic conductivity on the numerical results. Assuming a constant viscosity (i.e., isothermal condition) and density (i.e., low water pressure) of pore water [93], this analysis is equivalent to studying the influence of intrinsic permeability on the numerical results. For this purpose, we re-run the simulation in Section 5.2 with three different values of hydraulic conductivity: (a) $k = 3 \times 10^{-7}$ m/s, (b) $k = 3 \times 10^{-8}$ m/s, and (c) $k = 3 \times 10^{-9}$ m/s. Fig. 26 plots the reaction force versus the vertical displacement for the three simulations. Fig. 27 portrays the contour of pore water pressure at $u_y = 0.72$ mm for the three simulations. Fig. 28 presents the contours of equivalent plastic shear strains at $u_y = 0.72$ mm.

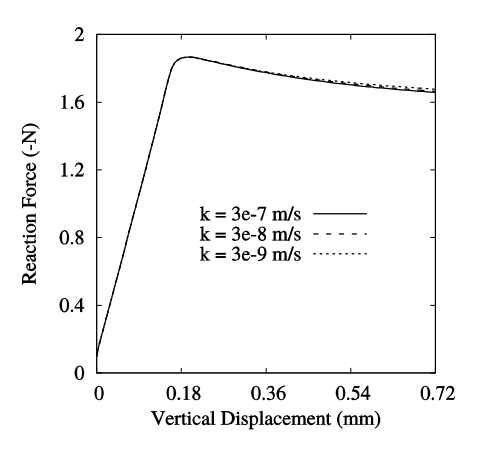


Fig. 26. Plot of reaction force versus vertical displacement for simulations with three values of hydraulic conductivity: (a) $k = 3 \times 10^{-7}$ m/s, (b) $k = 3 \times 10^{-8}$ m/s, and (c) $k = 3 \times 10^{-9}$ m/s.

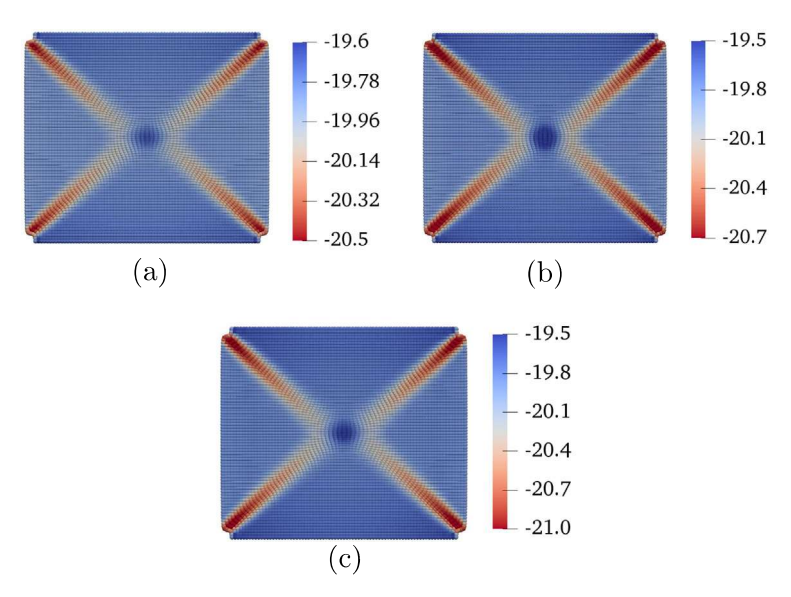


Fig. 27. Contours of pore water pressure (kPa) at $u_y = 0.72$ mm for simulations with three values of hydraulic conductivity: (a) $k = 3 \times 10^{-7}$ m/s, (b) $k = 3 \times 10^{-8}$ m/s, and (c) $k = 3 \times 10^{-9}$ m/s.

The contours of water pressure show that the hydraulic conductivity affects the magnitude of the water pressure in the post-localization regime. For example, the results in Fig. 27 the simulation with a smaller value of hydraulic conductivity generates a more considerable pressure change inside the shear band. Furthermore, the results in Fig. 28 show that the hydraulic conductivity has a negligible impact on the thickness of shear bands as well as the magnitude of equivalent plastic shear strain within the shear band. This observation may be due to the strong nonlocality for the fluid and solid phases in the coupled periporomechanics model. We note that the second-order work principle [106] can be used to study the characteristics of the localized shear zone of the simulations with the periporomechanics model. Recently the wave dispersion characteristics of peridynamics models for solids were examined by the spectral approach [107]. This feature could affect the solution of the periporomechanics model, although dynamics is not considered here. For future work, we will derive a nonlocal version of the second-order work principle and investigate the wave dispersion characteristics of the periporomechanics model [108].

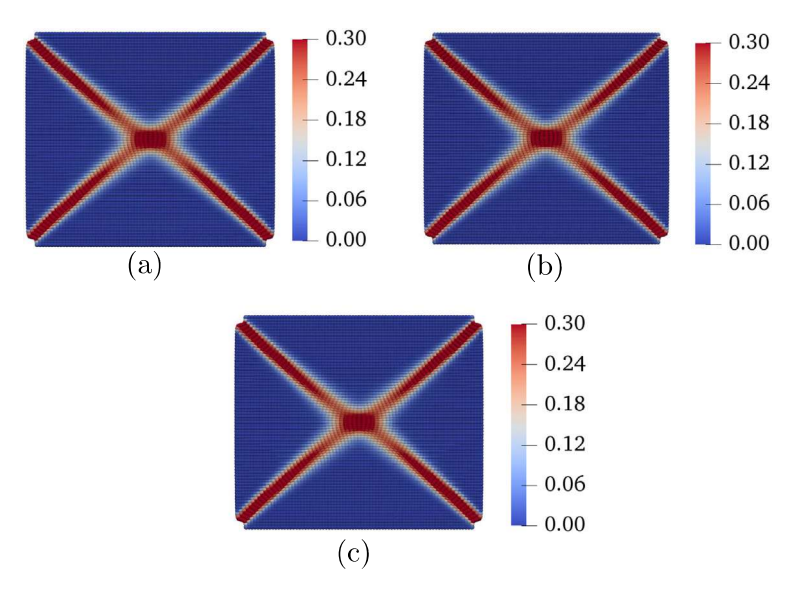


Fig. 28. Contours of equivalent plastic shear strain at $u_y = 0.72$ mm for simulations with three values of hydraulic conductivity: (a) $k = 3 \times 10^{-7}$ m/s, (b) $k = 3 \times 10^{-8}$ m/s, and (c) $k = 3 \times 10^{-9}$ m/s.

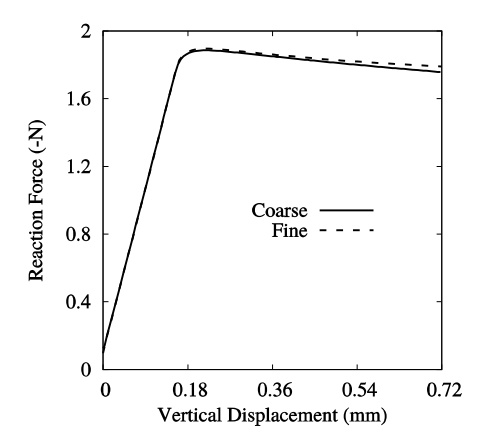


Fig. 29. Plot of reaction force versus vertical displacement with two different spatial discretization schemes.

5.2.3. Influence of spatial discretization

To examine the influence of spatial discretization on the numerical results, we rerun the simulation in Section 5.2 with two spatial discretization schemes: (a) the coarse one with 3200 material points ($\Delta x = 0.25$ mm) and (b) the fine one with 12,800 material points ($\Delta x = 0.125$ mm), respectively. To compare the results, the same horizon $\delta = 0.375$ mm is adopted for both simulations. Fig. 29 plots the reaction force over the vertical displacement at the top boundary for the simulations with two spatial discretization schemes. It is apparent that the force predicted in both simulations is almost identical.

Fig. 30 depicts the contours of water pressure superimposed on the deformed configuration at $u_y = 0.72$ mm. Fig. 31 plots the contours of equivalent plastic shear strains at $u_y = 0.72$ mm. The results in both figures evidence that the equivalent plastic shear strain and water pressure are insensitive to spatial discretizations. For both cases, the plastic shear deformation and the water pressure localize in a well-defined zone of finite thickness that is correlated to the horizon. It may be concluded that the proposed coupled periporomechanics is not sensitive to the spatial discretization, which is different from the standard finite element method. Thus, the proposed periporomechanics can be a valuable tool in the analysis of localization phenomena in unsaturated porous media.

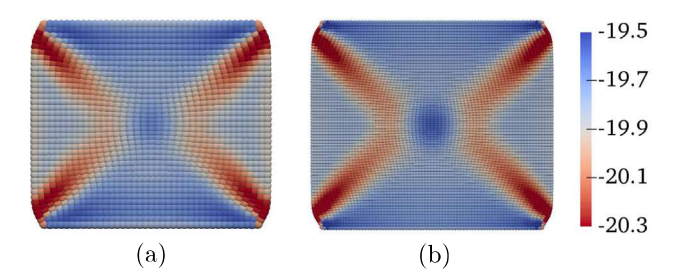


Fig. 30. Contours of pore water pressure (kPa) at $u_y = 0.72$ mm using (a) coarse discretization and (b) fine discretization in spatial domain.

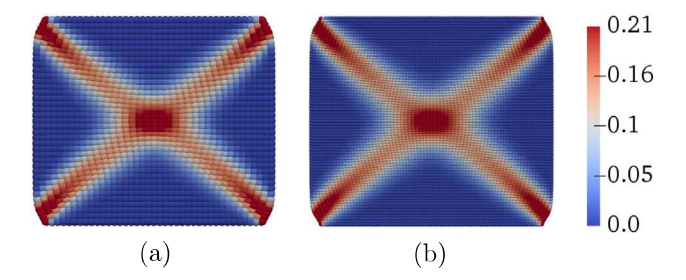


Fig. 31. Contours of equivalent plastic shear strains at $u_y = 0.72$ mm using (a) coarse discretization and (b) fine discretization in spatial domain.

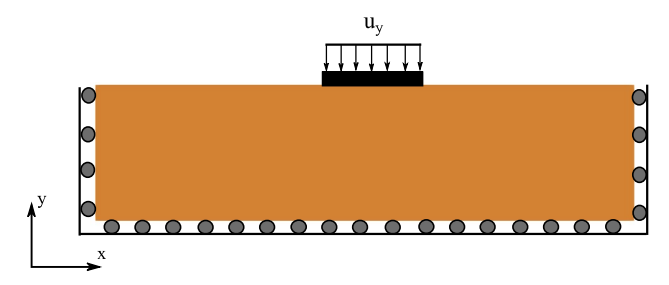


Fig. 32. Problem setup.

5.3. Example 3: Bearing capacity of a footing on unsaturated soils

This example deals with the bearing capacity of footing on unsaturated soils. Specifically, this example aims to show the proposed computational periporomechanics model can qualitatively simulate the localized failure mode of unsaturated soils under a footing. Fig. 32 sketches the geometry of the problem domain and the applied boundary conditions. A footing on which the displacement load is imposed is placed on the top of the soil domain. The dimensions of the soil domain are $4 \text{ m} \times 1 \text{ m} \times 0.02 \text{ m}$. The footing's dimensions are $0.8 \text{ m} \times 0.01 \text{ m} \times 0.02 \text{ m}$. As shown in Fig. 32, the lateral boundaries are constrained from horizontal deformation and are free to deform vertically. The bottom is constrained from vertical deformation. All fluid phase boundaries are impervious. The problem domain is discretized into 60,000 mixed material points. The multiphase length scale of δ is assumed 0.022 m.

The material parameters for the skeleton are as follows. Bulk modulus is 55.56×10^3 kPa, shear modulus is 18.52×10^3 kPa, swelling index is 0.05, critical state line slope is 1.0, compression index is 0.15, and specific volume at unit pre-consolidation pressure is 2.0, initial apparent pre-consolidation pressure is -200 kPa, and other parameters are the same as adopted in examples 1 and 2. The parameters for soil-water retention curve are $S_1 = 0.0$, $S_2 = 1.0$, $S_3 = 10$ kPa, $S_3 = 10$ kPa

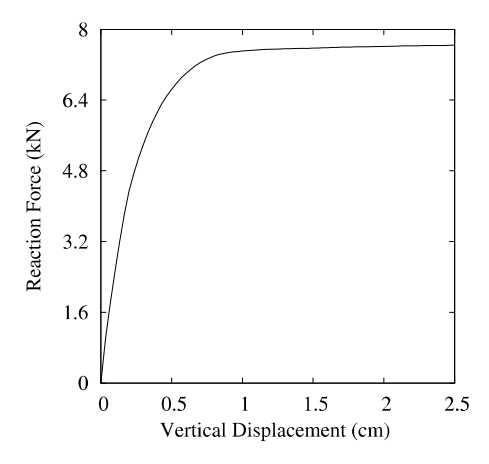


Fig. 33. Plot of the reaction force on the footing versus the applied vertical displacement.

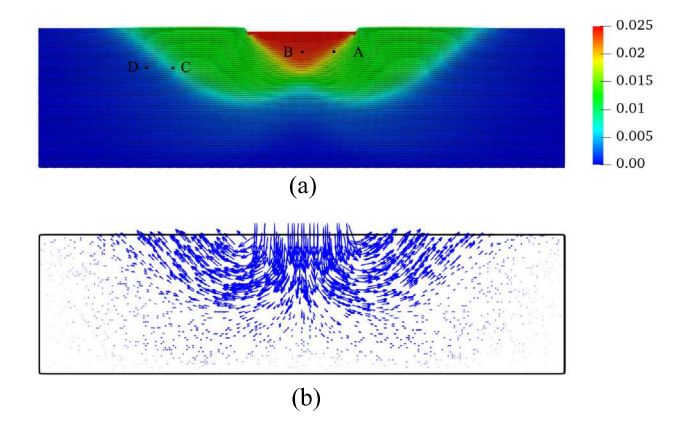


Fig. 34. Contour of (a) the magnitude and (b) direction of the displacement vector of the soil at $u_y = 2.5$ cm.

divided into two steps. In step 1, the soil's initial geostatic stress state is prescribed by imposing a gravity load on the soil. Then, a null deformation condition is assigned to the soil before a load is imposed on the footing. In step 2, the footing is given a vertical displacement $u_y = 0.04$ m at the constant rate of 1.67 mm/s in 15 s.

Fig. 33 plots the reaction force of the footing versus the vertical displacement. As shown in Fig. 33, the bearing capacity of the footing is around 7.5 kN. The contour of the magnitude of displacement is presented in Fig. 34(a). The displacement vector is plotted in Fig. 34(b) in which the arrowhead denotes the direction, and the length of the arrow tail shows the scaled magnitude. The contours of equivalent plastic shear strain, plastic volumetric strain (or plastic dilatation), pore water pressure in the soil at $u_y = 2.5$ cm are depicted in Fig. 35(a), (b) and (c). The results show that a typical localized shear failure mode of soil under shallow foundations [80]. For instance, the settlement of the footing has caused the formation of symmetric slip surfaces in the soil and soil upheaval on both sides of the footing. It is apparent from Fig. 35(b) that the shear bands under the footing are compactive while those associated with soil upheaval are dilatant. It is also revealed from Fig. 35(c) that matric suction decreases (pore pressure rises) in the compactive shear bands beneath the footing while matric suction increases in the dilative shear bands. The results are corroborated by the data shown in Figs. 36 and 37 which present the variation of the equivalent plastic strain and pore water pressure versus the footing's vertical displacement at points inside and outside the shear bands denoted in Fig. 34(a).

To test the solution's uniqueness, we rerun the simulation with a relatively finer spatial discretization consisting of 100,000 mixed material points. The same length scale and input parameters are adopted. The comparison between

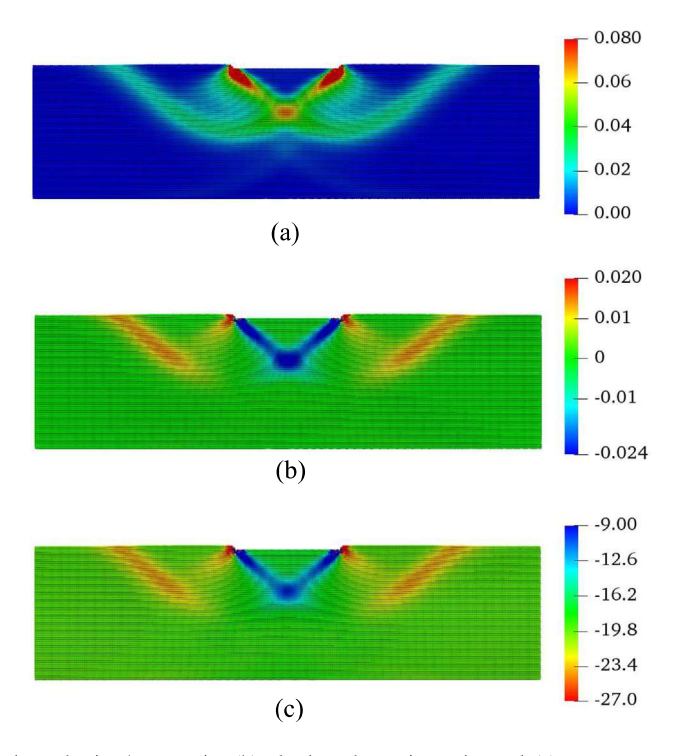


Fig. 35. Contours of (a) equivalent plastic shear strain, (b) plastic volumetric strain, and (c) pore water pressure (kPa) at $u_y = 2.5$ cm.

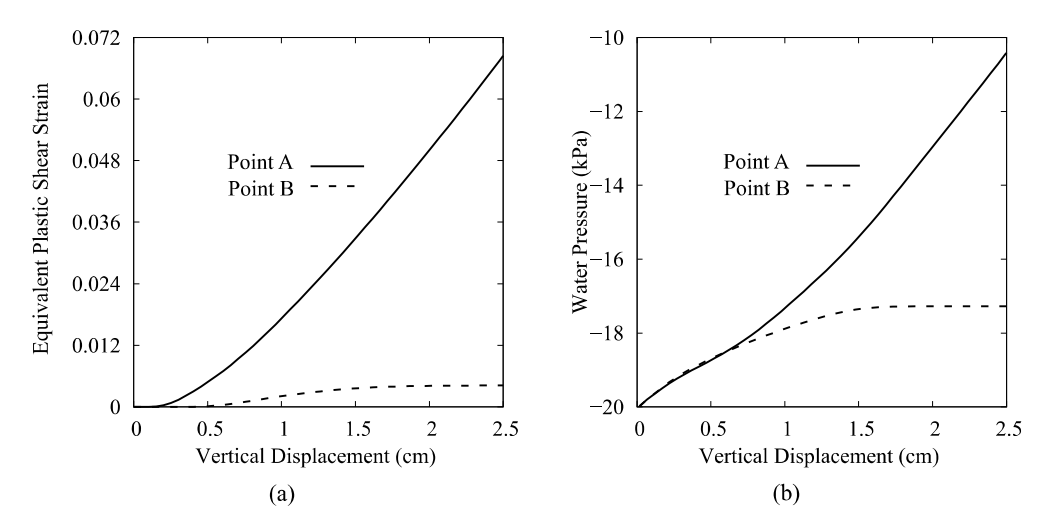


Fig. 36. Variation of (a) equivalent plastic shear strain and (b) pore water pressure versus the footing's vertical displacement at the points A and B (inside and outside banded compaction zones, respectively).

the two simulations is presented in Figs. 38–40. Here simulations I and II stand for the simulations with 60,000 and 100,000 material points respectively. Fig. 38 shows that the reaction force curves from both simulations are almost identical. Moreover, as shown in Figs. 39 and 40 respectively the contours of equivalent plastic shear strain and pore water pressure at $u_y = 2.5$ cm from both simulations are in good agreement. It is noted that all the numerical simulations are run in parallel on a supercomputer. To show the performance of the Open MPI implementation and scalability of the numerical code, the total wall-clock time for both simulations run in parallel with different number

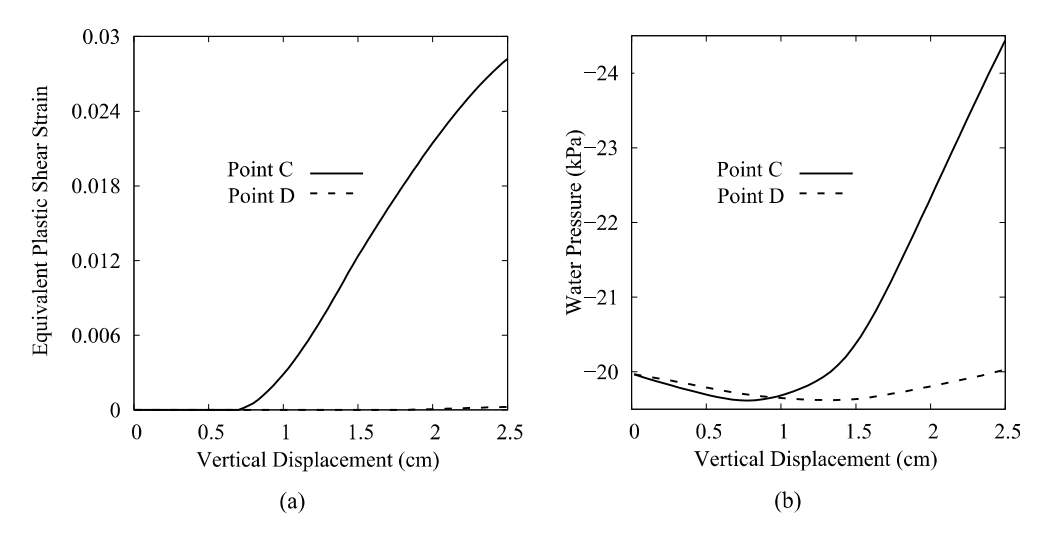


Fig. 37. Variation of (a) equivalent plastic shear strain and (b) pore water pressure at the points C and D versus the footing's vertical displacement (inside and outside banded dilation zones, respectively).

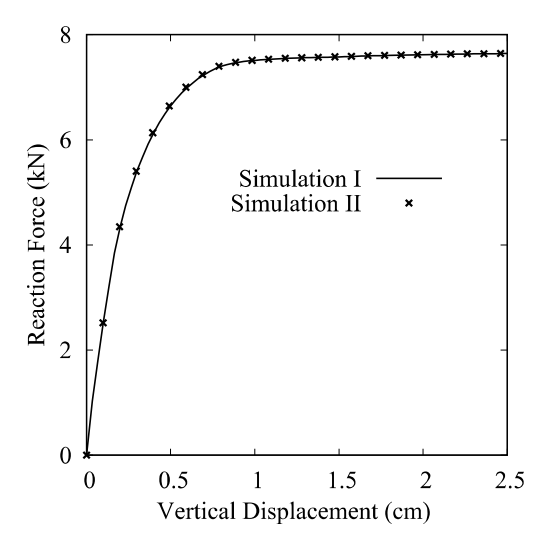


Fig. 38. Plot of reaction force on the footing over the applied vertical displacement for Simulation I and Simulation II.

Table 1
Comparison of wall-clock time for simulations I and II.

Number of CPU processors	Wall-clock Time	
	Simulation I (60,000 material points)	Simulation II (100,000 material points)
32	15,600 s	44,500 s
64	8900 s	33,000 s

of CPU (central processing unit) processors is summarized in Table 1. With the same number of CPU processors, the wall-clock time of simulation I with 60,000 multiphase material points is much shorter than that of simulation II with 100,000 multiphase material points. Doubling the number of CPU processors reduces the wall-clock time dramatically for both simulations, although the reduction of time is less than one half. The latter can be because more message passing occurs between processors for the simulations with 64 CPUs than those with 32 CPUs.

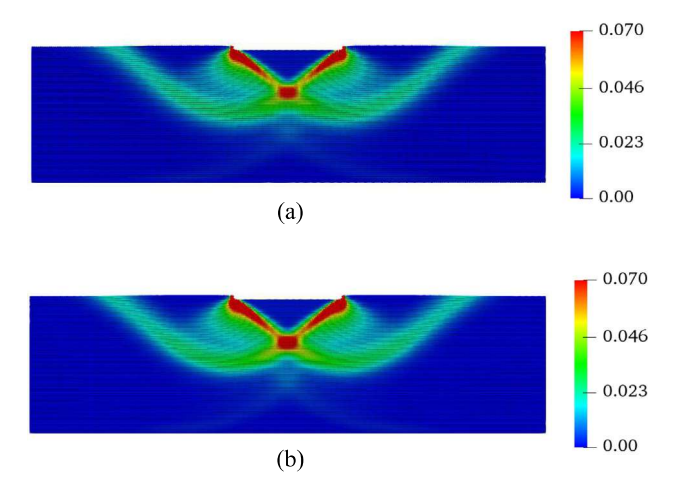


Fig. 39. Contours of equivalent plastic shear strain for (a) Simulation I and (b) Simulation II at $u_y = 2.5$ cm.

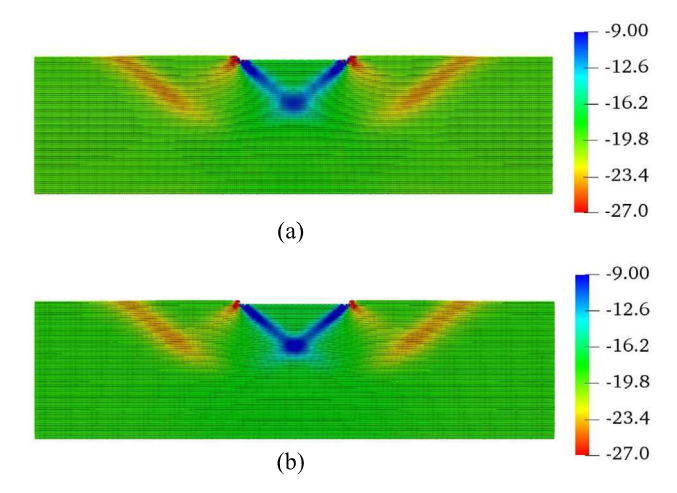


Fig. 40. Contours of pore water pressure for (a) Simulation I and (b) Simulation II at $u_y = 2.5$ cm.

6. Concluding remarks

In this article, we have implemented and validated a computational plastic periporomechanics model for simulating localized failure in unsaturated porous media assuming passive air pressure and incompressible solid grains. The effective force state concept [76] and the peridynamic state concept [50] are utilized in the coupled integro-differential equations that have an intrinsic length scale. The periporomechanics model can be used to account for both the discontinuity and nonlocality within the same mathematical framework. The formulation is restricted to small deformation under quasi-static condition. In the coupled plastic periporomechanics model, it is hypothesized that unsaturated porous media can be represented by a collection of mixed material points with infinitesimal volumes that have two kinds of degree of freedom (i.e., solid displacement and pore water pressure). In line with this hypothesis, an implicit multiphase Lagrangian meshless method is proposed to numerically implement the plastic periporomechanics model. The numerical implementation is validated by simulating Terzaghi's consolidation problem, drainage of a soil column, and Mandel's slab problem and comparing the numerical results against the analytical solutions and experimental data.

Numerical examples under different scenarios are conducted to establish the optimal performance of the computational plastic periporomechanics model for simulating strain localization in unsaturated porous media. It is shown that the intrinsic two-phase length scale can be utilized to characterize the finite thickness of the localization

of coupled solid deformation and unsaturated water flow. It is found from the numerical analysis that spatial discretization and hydraulic conductivity have mild effects on localized failure of unsaturated soils. This finding may be due to the fact that an identical length scale is adopted for both the pore fluid and solid skeleton. It is demonstrated from the footing example that the computational periporomechanics model can replicate the shear failure modes of unsaturated soils under a strip footing at the field scale.

Declaration of competing interest

The authors declare that they have no known competing financial interests or personal relationships that could have appeared to influence the work reported in this paper.

Acknowledgments

This work has been partially supported by the US National Science Foundation under contract numbers 1659932 and 1944009. The authors thank the anonymous reviewers for their expert reviews of this article. The authors are grateful to Professor Manolis Papadrakakis for his constructive comments and suggestions on the original version of this article.

Appendix. Summary of an elasto-plastic constitutive model for unsaturated soils

For self-completeness, the key components of a classical elastoplastic constitutive model are summarized as follows. The total strain in the rate form reads,

$$\dot{\varepsilon}_{ij} = \dot{\varepsilon}^e_{ij} + \dot{\varepsilon}^p_{ij},\tag{32}$$

where ε_{ij} is the total strain tensor, ε_{ij}^e is the elastic strain tensor, ε_{ij}^p is the plastic strain tensor, and i, j = 1, 2, 3. The effective stress is determined by the elastic model as

$$\dot{\bar{\sigma}}_{ij} = C^e_{ijkl} \dot{\varepsilon}^e_{kl},\tag{33}$$

where C_{ijkl}^e is the elastic stiffness tensor and k, l = 1, 2, 3.

$$C_{iikl}^{e} = (K - 2/3\mu)\delta_{ij}\delta_{kl} + \mu \left(\delta_{ik}\delta_{jl} + \delta_{il}\delta_{jk}\right),\tag{34}$$

where K and μ are the bulk and shear moduli of the solid skeleton, respectively. The plastic strain is determined by the plastic model. The yield surface is a function of the effective stress and the apparent pre-consolidation pressure \bar{p}_c and is expressed as

$$f(\bar{p}, q, \overline{p}_c) = \bar{p}(\bar{p} - \bar{p}_c) + \frac{q^2}{M^2},\tag{35}$$

where \bar{p} is the mean effective stress, \bar{p}_c is the apparent preconsolidation pressure, q is the deviator stress, and M is the slope of the critical state line. Here \bar{p} and q are determined by the following equations

$$\bar{p} = \frac{1}{3}\bar{\sigma}_{ij}\delta_{ij}$$
 and $q = \sqrt{\frac{3}{2}}\sqrt{s_{ij}s_{ij}}$. (36)

The size of the yield function is dependent on the apparent preconsolidation pressure, which is a function of the plastic volumetric strain ϵ_v^p , matric suction, and the degree of saturation [27]. The plastic strain rate is determined by

$$\dot{\varepsilon}_{ij}^{p} = \lambda \frac{\partial f}{\partial \bar{\sigma}_{ij}} = \lambda \left[\frac{1}{3} (2\bar{p} - \bar{p}_c) \delta_{ij} + \frac{2q}{M^2} \sqrt{\frac{3}{2}} \hat{n}_{ij} \right]$$
(37)

where λ is the plastic multiplier and $\hat{n}_{ij} = s_{ij} / \sqrt{s_{kl} s_{kl}}$.

References

- [1] J.W. Rudnicki, J. Rice, Conditions for the localization of deformation in pressure-sensitive dilatant materials, J. Mech. Phys. Solids 23 (6) (1975) 371–394.
- [2] I. Vardoulakis, J. Sulem, Bifurcation Analysis in Geomechanics, Blackie academic & professional, 1995.

- [3] J. Desrues, G. Viggiani, Strain localization in sand: an overview of the experimental results obtained in Grenoble using stereophotogrammetry, Int. J. Numer. Anal. Methods Geomech. 28 (4) (2004) 279–321.
- [4] A. Das, A. Tengattini, G.D. Nguyen, G. Viggiani, S.A. Hall, I. Einav, A thermomechanical constitutive model for cemented granular materials with quantifiable internal variables. Part II–validation and localization analysis, J. Mech. Phys. Solids 70 (2014) 382–405.
- [5] J.E. Andrade, C. Avila, S.A. Hall, N. Lenoir, G. Viggiani, Multiscale modeling and characterization of granular matter: from grain kinematics to continuum mechanics, J. Mech. Phys. Solids 59 (2) (2011) 237–250.
- [6] R.I. Borja, X. Song, A.L. Rechenmacher, S. Abedi, W. Wu, Shear band in sand with spatially varying density, J. Mech. Phys. Solids 61 (1) (2013) 219–234.
- [7] X. Song, K. Wang, M. Ye, Localized failure in unsaturated soils under non-isothermal conditions, Acta Geotech. 13 (1) (2018) 73–85.
- [8] N. Lu, J.W. Godt, Hillslope Hydrology and Stability, Cambridge University Press, 2013.
- [9] E.E. Alonso, Triggering and motion of landslides, Géotechnique (2020) 1-57.
- [10] H. Mühlhaus, I. Vardoulakis, The thickness of shear bands in granular materials, Geotechnique 37 (3) (1987) 271–283.
- [11] S. Nemat-Nasser, M. Hori, Micromechanics: Overall Properties of Heterogeneous Materials, Vol. 37, Elsevier, 1999.
- [12] K. Alshibli, A. Hasan, Spatial variation of void ratio and shear band thickness in sand using X-ray computed tomography, Géotechnique 58 (4) (2008) 249–257.
- [13] A. Tordesillas, D.M. Walker, E. Andò, G. Viggiani, Revisiting localized deformation in sand with complex systems, Proc. R. Soc. A 469 (2152) (2013) 20120606.
- [14] B. Schrefler, H. Zhang, L. Sanavia, Interaction between different internal length scales in strain localization analysis of fully and partially saturated porous media—the 1-D case, Int. J. Numer. Anal. Methods Geomech. 30 (1) (2006) 45–70.
- [15] H. Brandl, Energy foundations and other thermo-active ground structures, Géotechnique 56 (2) (2006) 81–122.
- [16] A. Gens, Soil-environment interactions in geotechnical engineering, Géotechnique 60 (1) (2010) 3-74.
- [17] E.E. Alonso, A. Gens, A. Josa, A constitutive model for partially saturated soils, Géotechnique 40 (3) (1990) 405-430.
- [18] N. Lu, W.J. Likos, Unsaturated Soil Mechanics, Wiley, 2004.
- [19] C.W.W. Ng, B. Menzies, Advanced Unsaturated Soil Mechanics and Engineering, CRC Press, 2014.
- [20] W. Ehlers, T. Graf, M. Ammann, Deformation and localization analysis of partially saturated soil, Comput. Methods Appl. Mech. Engrg. 193 (27–29) (2004) 2885–2910.
- [21] R.I. Borja, Cam-Clay plasticity. Part V: A mathematical framework for three-phase deformation and strain localization analyses of partially saturated porous media, Comput. Methods Appl. Mech. Engrg. 193 (48–51) (2004) 5301–5338.
- [22] X. Song, Transient bifurcation condition of partially saturated porous media at finite strain, Int. J. Numer. Anal. Methods Geomech. 41 (1) (2017) 135–156.
- [23] F. Oka, B. Shahbodagh, S. Kimoto, A computational model for dynamic strain localization in unsaturated elasto-viscoplastic soils, Int. J. Numer. Anal. Methods Geomech. 43 (1) (2019) 138–165.
- [24] K. Wang, X. Song, Strain localization in non-isothermal unsaturated porous media considering material heterogeneity with stabilized mixed finite elements, Comput. Methods Appl. Mech. Engrg. 359 (2020) 112770.
- [25] T.J. Hughes, The Finite Element Method: Linear Static and Dynamic Finite Element Analysis, Courier Corporation, 2000.
- [26] O.C. Zienkiewicz, A. Chan, M. Pastor, B. Schrefler, T. Shiomi, Computational Geomechanics, Citeseer, 1999.
- [27] R.I. Borja, X. Song, W. Wu, Critical state plasticity. Part VII: Triggering a shear band in variably saturated porous media, Comput. Methods Appl. Mech. Engrg. 261 (2013) 66–82.
- [28] X. Song, R.I. Borja, Finite deformation and fluid flow in unsaturated soils with random heterogeneity, Vadose Zone J. 13 (5) (2014).
- [29] M. Lazari, L. Sanavia, B. Schrefler, Local and non-local elasto-viscoplasticity in strain localization analysis of multiphase geomaterials, Int. J. Numer. Anal. Methods Geomech. 39 (14) (2015) 1570–1592.
- [30] X. Song, R.I. Borja, Mathematical framework for unsaturated flow in the finite deformation range, Internat. J. Numer. Methods Engrg. 97 (9) (2014) 658–682.
- [31] X. Song, M. Ye, K. Wang, Strain localization in a solid-water-air system with random heterogeneity via stabilized mixed finite elements, Internat. J. Numer. Methods Engrg. (2017).
- [32] R. De Borst, L. Sluys, H.-B. Muhlhaus, J. Pamin, Fundamental issues in finite element analyses of localization of deformation, Eng. Comput. 10 (2) (1993) 99–121.
- [33] A. Needleman, Material rate dependence and mesh sensitivity in localization problems, Comput. Methods Appl. Mech. Engrg. 67 (1)
- [34] Z.P. Bažant, M. Jirásek, Nonlocal integral formulations of plasticity and damage: survey of progress, J. Eng. Mech. 128 (11) (2002) 1119–1149.
- [35] N. Moës, T. Belytschko, Extended finite element method for cohesive crack growth, Eng. Fract. Mech. 69 (7) (2002) 813-833.
- [36] C. Miehe, M. Hofacker, F. Welschinger, A phase field model for rate-independent crack propagation: Robust algorithmic implementation based on operator splits, Comput. Methods Appl. Mech. Engrg. 199 (45–48) (2010) 2765–2778.
- [37] C. Callari, F. Armero, A. Abati, Strong discontinuities in partially saturated poroplastic solids, Comput. Methods Appl. Mech. Engrg. 199 (23–24) (2010) 1513–1535.
- [38] T. Mohammadnejad, A. Khoei, Hydro-mechanical modeling of cohesive crack propagation in multiphase porous media using the extended finite element method, Int. J. Numer. Anal. Methods Geomech. 37 (10) (2013) 1247–1279.
- [39] W. Ehlers, C. Luo, A phase-field approach embedded in the theory of porous media for the description of dynamic hydraulic fracturing, Comput. Methods Appl. Mech. Engrg. 315 (2017) 348–368.
- [40] S.-N. Roth, P. Léger, A. Soulaïmani, Fully-coupled hydro-mechanical cracking using XFEM in 3D for application to complex flow in discontinuities including drainage system, Comput. Methods Appl. Mech. Engrg. 370 (2020) 113282.

- [41] Y. Heider, W. Sun, A phase field framework for capillary-induced fracture in unsaturated porous media: Drying-induced vs. hydraulic cracking, Comput. Methods Appl. Mech. Engrg. 359 (2020) 112647.
- [42] S.A. Silling, Origin and effect of nonlocality in a composite, J. Mech. Mater. Struct. 9 (2) (2014) 245–258.
- [43] L. Dormieux, D. Kondo, F.-J. Ulm, Microporomechanics, John Wiley & Sons, 2006.
- [44] W.G. Gray, C.T. Miller, Introduction to the Thermodynamically Constrained Averaging Theory for Porous Medium Systems, Springer, 2014.
- [45] J.H. Cushman, The Physics of Fluids in Hierarchical Porous Media: Angstroms to Miles, Vol. 10, Springer Science & Business Media, 2013.
- [46] M.L. Parks, R.B. Lehoucq, S.J. Plimpton, S.A. Silling, Implementing peridynamics within a molecular dynamics code, Comput. Phys. Comm. 179 (11) (2008) 777–783.
- [47] J.N. Israelachvili, Intermolecular and Surface Forces, Academic press, 2011.
- [48] X. Song, M.-C. Wang, Molecular dynamics modeling of a partially saturated clay-water system at finite temperature, Int. J. Numer. Anal. Methods Geomech. 43 (13) (2019) 2129–2146.
- [49] S.A. Silling, Reformulation of elasticity theory for discontinuities and long-range forces, J. Mech. Phys. Solids 48 (1) (2000) 175–209.
- [50] S.A. Silling, M. Epton, O. Weckner, J. Xu, E. Askari, Peridynamic states and constitutive modeling, J. Elasticity 88 (2) (2007) 151–184.
- [51] W. Gerstle, N. Sau, S. Silling, Peridynamic modeling of concrete structures, Nucl. Eng. Des. 237 (12-13) (2007) 1250-1258.
- [52] S.A. Silling, R.B. Lehoucq, Convergence of peridynamics to classical elasticity theory, J. Elasticity 93 (1) (2008) 13.
- [53] F. Bobaru, M. Yang, L.F. Alves, S.A. Silling, E. Askari, J. Xu, Convergence, adaptive refinement, and scaling in 1D peridynamics, Internat. J. Numer. Methods Engrg. 77 (6) (2009) 852–877.
- [54] S.A. Silling, R. Lehoucq, Peridynamic theory of solid mechanics, in: Advances in Applied Mechanics, Vol. 44, Elsevier, 2010, pp. 73–168.
- [55] S.A. Silling, Linearized theory of peridynamic states, J. Elasticity 99 (1) (2010) 85-111.
- [56] T.L. Warren, S.A. Silling, A. Askari, O. Weckner, M.A. Epton, J. Xu, A non-ordinary state-based peridynamic method to model solid material deformation and fracture, Int. J. Solids Struct. 46 (5) (2009) 1186–1195.
- [57] E. Madenci, E. Oterkus, Peridynamic Theory and its Applications, Springer, 2014.
- [58] F. Bobaru, J.T. Foster, P.H. Geubelle, S.A. Silling, Handbook of Peridynamic Modeling, CRC press, 2016.
- [59] C. Wu, B. Ren, A stabilized non-ordinary state-based peridynamics for the nonlocal ductile material failure analysis in metal machining process, Comput. Methods Appl. Mech. Engrg. 291 (2015) 197–215.
- [60] S.A. Silling, Stability of peridynamic correspondence material models and their particle discretizations, Comput. Methods Appl. Mech. Engrg. 322 (2017) 42–57.
- [61] S.R. Chowdhury, P. Roy, D. Roy, J. Reddy, A modified peridynamics correspondence principle: Removal of zero-energy deformation and other implications, Comput. Methods Appl. Mech. Engrg. 346 (2019) 530–549.
- [62] N.A. Hashim, W. Coombs, C. Augarde, G. Hattori, An implicit non-ordinary state-based peridynamics with stabilised correspondence material model for finite deformation analysis, Comput. Methods Appl. Mech. Engrg. 371 (2020) 113304.
- [63] H. Zhang, P. Qiao, Virtual crack closure technique in peridynamic theory, Comput. Methods Appl. Mech. Engrg. 372 (2020) 113318.
- [64] T. Bode, C. Weißenfels, P. Wriggers, Peridynamic Petrov-Galerkin method: a generalization of the peridynamic theory of correspondence materials, Comput. Methods Appl. Mech. Engrg. 358 (2020) 112636.
- [65] D.Z. Turner, A non-local model for fluid-structure interaction with applications in hydraulic fracturing, Int. J. Comput. Methods Eng. Sci. Mech. 14 (5) (2013) 391–400.
- [66] X. Lai, B. Ren, H. Fan, S. Li, C. Wu, R.A. Regueiro, L. Liu, Peridynamics simulations of geomaterial fragmentation by impulse loads, Int. J. Numer. Anal. Methods Geomech. 39 (12) (2015) 1304–1330.
- [67] R. Jabakhanji, R.H. Mohtar, A peridynamic model of flow in porous media, Adv. Water Resour. 78 (2015) 22-35.
- [68] H. Ouchi, A. Katiyar, J. York, J.T. Foster, M.M. Sharma, A fully coupled porous flow and geomechanics model for fluid driven cracks: a peridynamics approach, Comput. Mech. 55 (3) (2015) 561–576.
- [69] S. Oterkus, E. Madenci, E. Oterkus, Fully coupled poroelastic peridynamic formulation for fluid-filled fractures, Eng. Geol. 225 (2017) 19–28
- [70] X. Song, N. Khalili, A peridynamics model for strain localization analysis of geomaterials, Int. J. Numer. Anal. Methods Geomech. (2018).
- [71] X. Song, S. Menon, Modeling of chemo-hydromechanical behavior of unsaturated porous media: a nonlocal approach based on integral equations, Acta Geotech. (2018) 1–21.
- [72] S. Menon, X. Song, Coupled analysis of desiccation cracking in unsaturated soils through a non-local mathematical formulation, Geosciences 9 (10) (2019) 428.
- [73] H. Zhang, H. Li, H. Ye, Y. Zheng, A coupling peridynamic approach for the consolidation and dynamic analysis of saturated porous media, Comput. Mech. 64 (4) (2019) 1097–1113.
- [74] T. Ni, F. Pesavento, M. Zaccariotto, U. Galvanetto, Q.-Z. Zhu, B.A. Schrefler, Hybrid FEM and peridynamic simulation of hydraulic fracture propagation in saturated porous media, Comput. Methods Appl. Mech. Engrg. 366 (2020) 113101.
- [75] A. Katiyar, J.T. Foster, H. Ouchi, M.M. Sharma, A peridynamic formulation of pressure driven convective fluid transport in porous media, J. Comput. Phys. 261 (2014) 209–229.
- [76] X. Song, S.A. Silling, On the peridynamic effective force state and multiphase constitutive correspondence principle, J. Mech. Phys. Solids 145 (2020) 104161.
- [77] S.A. Silling, E. Askari, A meshfree method based on the peridynamic model of solid mechanics, Comput. Struct. 83 (17–18) (2005) 1526–1535.

- [78] W. Gropp, E. Lusk, N. Doss, A. Skjellum, A high-performance, portable implementation of the MPI message passing interface standard, Parallel Comput. 22 (6) (1996) 789–828.
- [79] E. Gabriel, G.E. Fagg, G. Bosilca, T. Angskun, J.J. Dongarra, J.M. Squyres, V. Sahay, P. Kambadur, B. Barrett, A. Lumsdaine, et al., Open MPI: Goals, concept, and design of a next generation MPI implementation, in: European Parallel Virtual Machine/Message Passing Interface Users' Group Meeting, Springer, 2004, pp. 97–104.
- [80] K. Terzaghi, Theoretical Soil Mechanics, Chapman And Hall, Limited., London, 1951.
- [81] A.C. Liakopoulos, Transient Flow through Unsaturated Porous Media (Ph.D. thesis), University of California, Berkeley, 1964.
- [82] J. Mandel, Consolidation des sols (étude mathématique), Geotechnique 3 (7) (1953) 287–299.
- [83] H. Zhang, L. Sanavia, B. Schrefler, An interal length scale in dynamic strain localization of multiphase porous media, Mech. Cohesive-Frict. Mater.: Int. J. Exp. Model. Comput. Mater. Struct. 4 (5) (1999) 443–460.
- [84] R. De Borst, L. Sluys, Localisation in a Cosserat continuum under static and dynamic loading conditions, Comput. Methods Appl. Mech. Engrg. 90 (1–3) (1991) 805–827.
- [85] H. Zhang, L. Sanavia, B. Schrefler, Numerical analysis of dynamic strain localisation in initially water saturated dense sand with a modified generalised plasticity model, Comput. Struct. 79 (4) (2001) 441–459.
- [86] D.G. Fredlund, H. Rahardjo, Soil Mechanics for Unsaturated Soils, John Wiley & Sons, 1993.
- [87] R.W. Lewis, B.A. Schrefler, The Finite Element Method in the Static and Dynamic Deformation and Consolidation of Porous Media. BOOK, John Wiley, 1998.
- [88] M. Nuth, L. Laloui, Effective stress concept in unsaturated soils: Clarification and validation of a unified framework, Int. J. Numer. Anal. Methods Geomech. 32 (7) (2008) 771–801.
- [89] N. Lu, J.W. Godt, D.T. Wu, A closed-form equation for effective stress in unsaturated soil, Water Resour. Res. 46 (5) (2010).
- [90] J. Cao, J. Jung, X. Song, B. Bate, On the soil water characteristic curves of poorly graded granular materials in aqueous polymer solutions, Acta Geotech. 13 (1) (2018) 103–116.
- [91] M.T. Van Genuchten, A closed-form equation for predicting the hydraulic conductivity of unsaturated soils, Soil Sci. Am. J. 44 (5) (1980) 892–898.
- [92] O. Coussy, Poromechanics, John Wiley & Sons, 2004.
- [93] J. Bear, Dynamics of Fluids in Porous Media, Courier Corporation, 2013.
- [94] M. Gunzburger, R.B. Lehoucq, A nonlocal vector calculus with application to nonlocal boundary value problems, Multiscale Model. Simul. 8 (5) (2010) 1581–1598.
- [95] S. Silling, EMU User's Manual, Sandia National Laboratories, Albuquerque, NM, 2006.
- [96] G.-R. Liu, Y.-T. Gu, An Introduction to Meshfree Methods and their Programming, Springer Science & Business Media, 2005.
- [97] T. Ni, M. Zaccariotto, Q.-Z. Zhu, U. Galvanetto, Coupling of FEM and ordinary state-based peridynamics for brittle failure analysis in 3D, Mech. Adv. Mater. Struct. 28 (9) (2021) 875–890.
- [98] M. Zaccariotto, T. Mudric, D. Tomasi, A. Shojaei, U. Galvanetto, Coupling of FEM meshes with Peridynamic grids, Comput. Methods Appl. Mech. Engrg. 330 (2018) 471–497.
- [99] Y. Tong, W.-Q. Shen, J.-F. Shao, An adaptive coupling method of state-based peridynamics theory and finite element method for modeling progressive failure process in cohesive materials, Comput. Methods Appl. Mech. Engrg. 370 (2020) 113248.
- [100] J.C. Simo, T.J. Hughes, Computational Inelasticity, Vol. 7, Springer Science & Business Media, 1998.
- [101] R. Nova, R. Castellanza, C. Tamagnini, A constitutive model for bonded geomaterials subject to mechanical and/or chemical degradation, Int. J. Numer. Anal. Methods Geomech. 27 (9) (2003) 705–732.
- [102] R.I. Borja, Plasticity: Modeling & Computation, Springer Science & Business Media, 2013.
- [103] C. Tamagnini, M.O. Ciantia, Plasticity with generalized hardening: constitutive modeling and computational aspects, Acta Geotech. 11 (3) (2016) 595–623.
- [104] C. Cryer, A comparison of the three-dimensional consolidation theories of Biot and Terzaghi, Quart. J. Mech. Appl. Math. 16 (4) (1963) 401–412.
- [105] A. Verruijt, Theory and Problems of Poroelasticity, Vol. 71, Delft University of Technology, 2013.
- [106] E. Mikaeili, B. Schrefler, XFEM, strong discontinuities and second-order work in shear band modeling of saturated porous media, Acta Geotech. 13 (6) (2018) 1249–1264.
- [107] Z.P. Bažant, W. Luo, V.T. Chau, M.A. Bessa, Wave dispersion and basic concepts of peridynamics compared to classical nonlocal damage models, J. Appl. Mech. 83 (11) (2016).
- [108] S.A. Silling, Attenuation of waves in a viscoelastic peridynamic medium, Math. Mech. Solids 24 (11) (2019) 3597-3613.